Applied Catalysis B: Environmental 341 (2024) 123282

Contents lists available at ScienceDirect

Applied Catalysis B: Environmental

journal homepage: www.elsevier.com/locate/apcatb

In situ topotactic formation of the *pn*-type inorganic intergrowth bulk heterojunction NiO(Al)/CuO(Ni,Al) for photocatalytic CO_2 methanation

Yuexian Li [a], Wenli Su [c], Yusen Yang [a], Lianxia Bai [a], Jun Lu [a,b,*], Wenkai Zhang [c,**], Shuo Wei [d,**]

[a] State Key Laboratory of Chemical Resource Engineering and College of Chemistry, Beijing University of Chemical Technology, P. Box 98, Beisanhuan East Road 15, Beijing 100029, PR China

[b] Beijing Advanced Innovation Center for Soft Matter Science and Engineering, Beijing University of Chemical Technology, P. Box 98, Beisanhuan East Road 15, Beijing 100029, PR China

[c] Department of Physics and Applied Optics Beijing Area Major Laboratory, Center for Advanced Quantum Studies, Beijing Normal University, Xinjiekou Outside Street 19, Beijing 100875, PR China

[d] College of Chemistry, Beijing Normal University, Xinjiekou Outside Street 19, Beijing 100875, PR China

ARTICLE INFO

Keywords:
pn inorganic intergrowth bulk heterojunction
Solid solution
Two-stage topological pyrolysis
Structural memory effects
CO_2 methanation

ABSTRACT

Considering that photosynthetic CH_4 seems to have a high energy density, it serves as a powerful way for storing renewable energy. In this work, a potential *pn*-type inorganic intergrowth bulk heterojunction (*pn*-IIBH) NiO(Al)/CuO(Ni,Al) was designed and obtained by the precursor CuNiAl-layered double hydroxides with two-stage topological pyrolysis (TTP) method. The microstructure was investigated in detail EXAFS to understand in-situ topotactic formation of the IIBH. Then, by using ISI-XPS, and fs-TAS, the transfer mechanism of the photogenerated electrons in NiO(Al)/CuO(Ni,Al) was explored which met *pn*-type heterojunction. Furthermore, it was screened for CO_2 photoreduction to target CH_4 (86.59 μmol/g·h) and O_2 (150.84 μmol/g·h) from H_2O and the selectivity of CH_4 reached more than 87.13%. Finally, in-situ IR and DFT calculation demonstrated that CO_2 methanation by the hydrogenation pathway occurred and the Ni doping in the *pn*-IIBH activated CO_2 adsorption more effectively. This work offers an approach to photocatalysis development in CO_2 methanation.

1. Introduction

Energy and environmental issues are becoming increasingly relevant as the industrialization process continues [1]. As a result, artificial methane (CH_4) photosynthesis technology offers a potential solution to these difficulties inspired by natural photosynthesis [2–4]. The following reaction generalized this complex chemical process [5–7]:

$$CO_2 + 2H_2O \rightarrow CH_4 + 2O_2 \quad (1)$$

Photosynthetic methane serves as an effective medium for renewable energy storage due to its high energy density. However, this reaction is endothermic and has a substantial positive Gibbs energy change (ΔG^{θ} (298 K) = 818 kJ mol^{-1}), hence it cannot occur spontaneously under ordinary circumstances [8,9]. To guarantee the smooth methanation of CO_2 and the oxidation of H_2O at mild condition, a catalyst and energy input are needed to minimize the activation energy. Different photocatalysts, such as TiO_2 [10–12], $Zn_xCd_{1-x}S$ [13], g-C_3N_4 [14,15], and graphene, have been developed in recent decades to enhance CO_2 methanation conversion rates. Y. Wang et al. [16], for example, used a SiC@MoS_2 nanoflower without sacrificial reagents to convert CO_2 to CH_4 under visible light irradiation. However, few photocatalysts have been able to reduce CO_2 to CH_4 and oxidize H_2O to O_2 concurrently, which demands not only quick photogenerated electron and hole transfers to the catalyst surface but also the matched rapid surface reactions. Simple semiconductor catalysts are incapable of fulfilling these demands up to now [17–20]. The construction of heterojunctions is one of the most efficient methods for both optimizing the migration path of photogenerated carriers and enabling photocatalytic reactions at different active sites [21]. Based on the migration paths taken by photogenerated carriers, heterojunctions with staggered gaps may also be

* Correspondence to: State Key Laboratory of Chemical Resource Engineering and College of Chemistry/Beijing Advanced Innovation Center for Soft Matter Science and Engineering, Beijing University of Chemical Technology, P. Box 98, Beisanhuan East Road 15, Beijing 100029, PR China.

** Corresponding authors.

E-mail addresses: lujun@mail.buct.edu.cn (J. Lu), wkzhang@bnu.edu.cn (W. Zhang), vshuo@bnu.edu.cn (S. Wei).

https://doi.org/10.1016/j.apcatb.2023.123282
Received 27 June 2023; Received in revised form 12 August 2023; Accepted 8 September 2023
Available online 9 September 2023
0926-3373/© 2023 Elsevier B.V. All rights reserved.

divided into II-type, Z-scheme, and S-scheme heterojunctions. In traditional II-type heterojunctions, photogenerated electrons at the higher level of the conduction band (CB) edges migrate to the lower level of the CB, while photogenerated holes at the lower edges of the valence band (VB) edges migrate to the higher level of the VB edges [22]. As for Z-scheme heterojunctions, photogenerated electrons at the lower level CB edges may go to the higher level VB edges and recombine with holes [23]. The majority of an S-scheme heterojunctions is constituted of two n-type semiconductors, one of which is a reduced semiconductor with a small work function and a high Fermi energy level, and the other of which is an oxidized semiconductor with a large work function and a low Fermi energy level, constitute [24]. It is noteworthy that a number of studies have shown that staggered gap heterojunctions based on the combination of *p*-type and *n*-type semiconductors have photogenerated carrier migration paths similar to those of II-type heterojunctions but can increase photocatalytic activity more effectively [21], which is primarily related to the presence of the built-in electric field, such as CuO-TiO_2 [25], RuO_2/TiO_2 [26], NiO/In_2O_3 [27], NiIn-LDH/In_2S_3 [28], Ag/Cu_2O@rGO [29], $Mo_2C/Bi_4O_5Br_2$ [30], NiAl-LDH/g-C_3N_4 [31], $Zn_xCd_{1-x}S$/Au@ g-C_3N_4 [13], and so on. Therefore, to solve the problem, we also propose employing a novel *pn*-type inorganic intergrowth bulk heterojunctions (*pn*-IIBH) to enhance the separation of photogenerated carriers, which may be favorable for the subsequently reaction on the respective semiconductor domain. It is worth noting that this is distinct from the traditional *p-n* plane heterojunction (PH) [32,33], which is built by straightforward physical grinding preparation [28, 34–36] or epitaxial growth of one semiconductor as the foundation of another one [36,37]. The intrinsic restrictions of the solid-state reaction might result in inadequate contact between semiconductor surfaces and develop into various traps for photogenerated carriers and restricting the catalyst activity. On the other hand, bulk heterojunction (BH) [38, 39], which was first proposed by Heeger et al. [40,41], Nobel Laureates in Chemistry in 1995, mixed acceptor and donor organic semiconductors forming an optimal interpenetrating network at the nanoscale to ensure that the distance between photogenerated carriers, and charge separation interface is within a carrier diffusion length and more donor-acceptor interfaces, effectively fixing the problem of poor contact at the PH interface in organic semiconductors [42,43]. Is it to be possible to manufacture *p-n* type heterojunctions of inorganic semiconductors, as inspired by organic BH, to apply to CO_2 photocatalytic reduction? The relative crystallinity and miscibility of the donor-acceptor affect the phase separation in the organic BH design, which consists of two parts [44–47]: one for the crystalline region to generate electrons, and another part for the mixed-phase region to contribute to charge separation.

Layered double hydroxides (LDHs) as the representative two-dimensional (2D) layered nanomaterials have special structural memory effects (SME) [48–50]. It simply means that when calcination temperature of LDHs is below 500 ℃, LDHs will lose interlayer water, anions and hydroxyl groups to form mixed metal oxide (MMO). While exposed the MMO in alkaline conditions (such as carbonate solution), the layered LDHs structure can recover with the feature of structural topological transformation. However, it is worth mentioning that the SME is indeed not present in all LDHs. For example, Q. Meng et al. [51] showed that NiAl-LDHs, MgAl-LDHs and MgFe-LDHs have SME, while ZnAl-LDHs have no SME. J. Li et al. [48] demonstrated by in situ NMR spectroscopy that the process of SME from MgAl-MMO to MgAl-LDHs follows the mechanism of dissolution-recrystallization. Currently, the SME of LDHs is used to prepare catalysts mainly based on their recovery intercalation properties for photocatalytic degradation of dyes [52,53], and the specific catalysts are listed in SI (Table S1). We use the difference in the structural memory effect of different LDHs, specifically, whether the MMO formed after calcination of different LDHs can recover back to the LDHs structure to construct heterojunctions. Therefore, by exploiting the SME of LDHs, we expect that it is possible to construct electron-hole generating crystalline domains and charge-transporting domains comparable to those in organic BH.

In this paper, we propose to build *pn*-IIBH: NiO(Al)/CuO(Ni,Al) by a novel approach named two-stage topological pyrolysis (TTP) based on the SME of NiAl-LDHs, which was shown in Scheme 1 and prepared it indeed. Without the electron sacrifice reagent, we screened it for CO_2 photocatalytic reduction for CH_4 production (68.59 μmol/g·h) and O_2 overflow (150.84 μmol/g·h) with stoichiometric ratio, and the selectivity of CH_4 reached more than 87.13%. The topological transformation mechanism, photogenerated electron transfer mechanism, and the reason for high CH_4 selectivity from the *pn*-IIBH structure were discussed in-depth.

2. Experimental section

2.1. Synthesis of CuNiAl-LDHs precursor

CuNiAl-LDHs were synthesized by the most common coprecipitation method with a constant pH value. 0.02 mol cupric nitrate hexahydrate ($Cu(NO_3)_2{\cdot}6H_2O$), 0.02 mol nickel nitrate hexahydrate ($Ni(NO_3)_2{\cdot}6H_2O$), and 0.01 mol aluminum nitrate hexahydrate ($Al(NO_3)_3{\cdot}9H_2O$) were dissolved in 100 mL deionized water, denoted as solution A. 0.1 mol NaOH ($n^{-}_{NaOH} = 2(n^{2+}_{M} + n^{3+}_{M})$) and 0.02 mol Na_2CO_3 ($n^{2-}_{CO3} = 2\ n^{3+}_{M}$) were weighed and dissolved in 100 mL deionized water, denoted as solution B. Added 20 mL deionized water into 500 mL round-bottomed flask, and used a peristaltic pump to drop liquid A and liquid B simultaneously into the round-bottomed flask at a certain speed slowly. During the whole process, pH was kept at about 8–8.5 to ensure that all metal ions precipitated simultaneously, and the products were collected after crystallization for 6 h in 65 ℃ water bath. Finally, the products were washed with deionized water and ethanol 3 times, respectively, and freeze-dried for 12 h to obtain CuNiAl-LDHs powder. For exploring the effects of different molar ratio of Cu^{2+} and Ni^{2+} ions on the preparation of *pn*-IIBH, CuNiAl-LDHs were synthesized by changing the molar ratios of Cu^{2+}, Ni^{2+}, and Al^{3+}. (Cu^{2+}: Ni^{2+}: Al^{3+} = 1:1:1, 1:2:1, 1:3:1, 2:2:1). Similarly, the synthesis method of NiAl-LDHs and CuAl-LDHs was consistent with the above method.

2.2. Synthesis of pn-IIBH: NiO(Al)/CuO(Ni,Al)

NiO(Al)/CuO(Ni,Al) was prepared by TTP. CuNiAl-LDHs powders with different molar ratios were placed in a crucible to calcine for 8 h in air at a muff furnace for 350 ℃ with a heating rate of 10 min·℃$^{-1}$, denoted as CuNiAl-MMO. The calcined CuNiAl-MMO was dispersed in 50 mL deionized water, and the solution pH was adjusted between 8 and 9 with 2 M Na_2CO_3 solution and stirred in 65 ℃ water bath for 6 h. Finally, it was washed with deionized water and ethanol 3 times, and placed in freeze-drying for 12 h, denoted as CuO(Ni,Al)@NiAl-LDHs. Finally, the above products were calcined at 350 ℃, 500 ℃, or 600 ℃ for the second time, denoted as NiO(Al)/CuO(Ni,Al).

3. Characterization

Crystal structure identification was investigated by Powder X-ray diffraction (XRD) using the Rigaku UItima III diffractometer with Cu Kα radiation (λ = 0.154 nm, 40 kV and 40 mA). The 2theta range was from 3° to 70° and the scan speed of 10° min^{-1}. The morphology of the photocatalysts was measured by scanning electron microscopy (SEM, Zeiss) and transmission electron microscopy (TEM, JEM-3010). The light absorption properties of the photocatalyst were analyzed by UV–Visible diffuse reflectometry (UV-DRS) using a Hitachi U-3900 H spectrophotometer at a scanning speed of 120 nm min^{-1} with white $BaSO_4$ as the reflection standard. The Fourier transform infrared spectrometer (FT-IR, TENSOR II) was used to determine the functional group of the samples. X-ray photoelectron spectroscopy (XPS) analysis was performed using Thermo Fisher Scientific ESCALAB 250, and the surface composition and chemical valence states were analyzed by using Al Kα

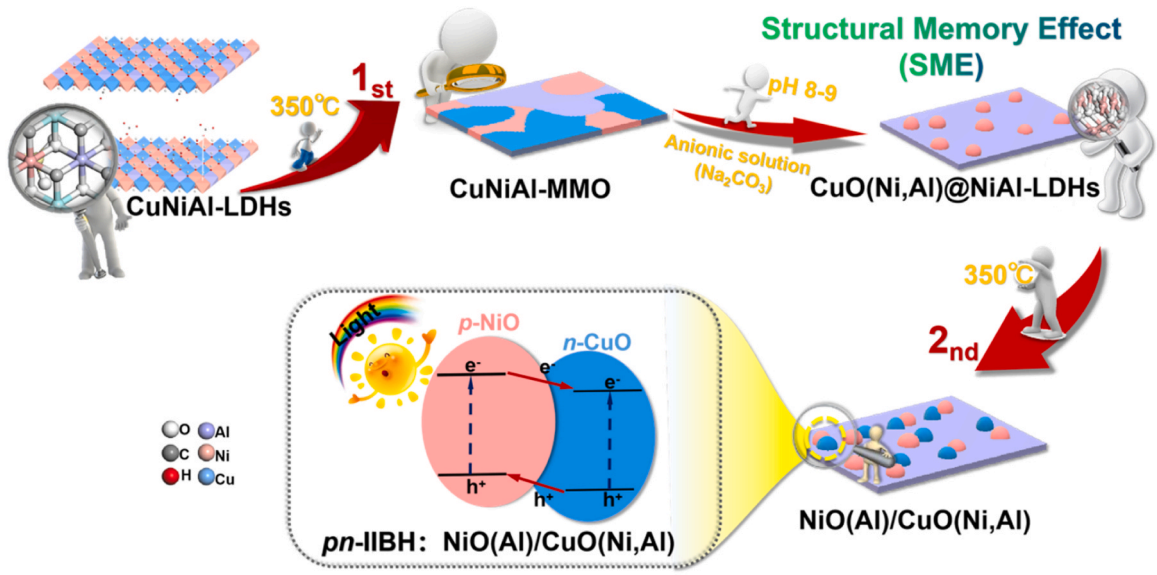

Scheme 1. The schematic diagram depicts the use of CuNiAl-LDHs as precursors for the construction of *pn*-IIBH NiO(Al)/CuO(Ni,Al) by the two-stage topological pyrolysis (TTP) method.

radiation (1486 eV). *In-situ* irradiation XPS measurements were conducted under the similar conditions except that UV–visible light irradiation was introduced. The PL spectra of all samples were studied by using the HITACHIF-4600 fluorescence spectrophotometer. Element content was determined by inductively coupled plasma-atomic emission spectra (ICP-AES, Agilent). Helios equipment was used to capture femtosecond transient absorption spectra (fs-TAS) of the samples as-prepared, and the nondegenerate pump-probe system was used to investigate the transient dynamics from 0.02 femtoseconds to 3.6 picosecond. The O PerA Solo optical parametric amplifier (Coherent Libra, 800 nm, 50 fs, 4 mJ) produced the 360 nm-pump pulses (5 mW average at tested samples), which were pumped by an LBO laser (Coherent Evolution-50 C, 1 kHz system). The amplifier was seeded using a mode locked Ti-sapphire oscillator (Coherent Vitesse, 80 MHz). The 800 nm-femtosecond pluses were pushed through a continuously spinning CaF_2 crystal to produce the white light continuum from 320 nm to 750 nm. The multiexponential decay function was used to fit the kinetic curves of the samples. X-ray absorption fine structure (XAFS) experiments were obtained by the Beijing Synchrotron Radiation Facility (BSRF) with the 1W1B beamline and a double crystal Si (111) monochromator.

4. Results and discussion

4.1. Synthesis and characterization of the photocatalyst

The formation of *pn*-IIBH NiO(Al)/CuO(Ni,Al) by a novel approach named the two-stage topological pyrolysis (TTP) method based on the structural memory effect, was displayed in Scheme 1. Firstly, the coprecipitation approach was used to obtain CuNiAl-LDHs precursors, and then it was calcined, at 350 °C in air for 8 h to obtain the poor crystalline CuNiAl-mixed metal oxide (CuNiAl-MMO). This product was subsequently suspended in Na_2CO_3 aqueous solution for 6 h to get the CuO(Ni,Al)@NiAl-LDH according to the structural memory effect, and then recalcined at 350 °C in air for 8 h to produce another CuNiAl-MMO nanocomposites, denoted as NiO(Al)/CuO(Ni,Al). The entire TTP process can be regarded as a topological transformation due to the layered structure without crystalline collapse significantly by scanning electron microscope (SEM) (Fig. S1) which will be illustrated in detail for the structural characterization below.

The X-ray diffraction (XRD) patterns (Fig. 1A) and Fourier transform infrared spectra (FTIR) (Fig. S2) of CuNiAl-LDHs showed that all the diffraction peaks and vibration signals were assigned to the CuNiAl-CO_3-LDHs [54–56] The Raman spectra (Fig. 1B) displayed the distinct bands at ~1050 and ~500 cm^{-1}, often observed in the Ni-based LDHs [57,58]. After the first calcination of CuNiAl-LDHs, the Bragg peaks of 00 *l* (*l* = 3, 6, 9) vanished (Fig. 1A), while three broad weak peaks arise at 37.4°, 43.7°, and 63.3°, which can be attributed to NiO-like phase with a higher angle shift due to solid solution nature of CuNiAl-MMO, which is locally distorted relative to the original crystal. The *R*-space plots of CuNiAl-LDHs and CuNiAl-MMO in extend X-ray absorption fine structure (EXAFS) indicated that the coordination numbers of Cu (Fig. 1C) and Ni (Fig. S3) were basically unchanged during the first pyrolysis, both in hexacoordinated octahedra of M-O and M-O-M (M = Cu, Ni) shells. It is worth noting that the coordination environment of CuNiAl-MMO was somewhat different from that of pure CuO and NiO, and the standard Cu-O-Cu1 and Cu-O-Cu2 shells in pure CuO did not appear in the solid solution (Fig. 1C).

When the NiAl-LDHs were recovered from the CuNiAl-MMO, the lamellar diffraction peaks in XRD (Fig. 1A) and the vibrational peaks of CO_3^{2-} in FTIR [59] (Fig. S2) reappear. Something interesting has come up that CuO-like phase crystallized and coexisted with the NiAl-LDHs, which was nominated as CuO(Ni,Al)@NiAl-LDHs. The Raman spectra (Fig. 1B) also showed the distinct bands at ~1056 and ~532 cm^{-1}, matching with the Ni-based LDHs [57,58]. The *R*-space plots of CuO(Ni,Al)@NiAl-LDHs in EXAFS (Fig. 1C) indicated that there were Cu-O-Cu1 and Cu-O-Ni shells. The coordination number of Cu changed from about 6–5 (Fig. 1D), while the coordination number of Ni remained the same. Such a phenomenon is consistent with the previously reported results that NiAl-LDHs have the typical structural memory effect while CuAl-LDHs can not easy to form due to the Jahn-Teller effect of Cu^{2+} [60].

When undergoing the second calcination at 350 °C, the main diffraction peaks in Fig. 1E can be indexed as monoclinic crystalline CuO (JPCDS# 48–1548) and cubic crystalline NiO (JPCDS# 44–1159). The microstructure details were probed by High-resolution transmission electron microscope (HRTEM) and the phase interfaces were found within many crystallites. One of the images was shown in Fig. 1F and the phase interface of NiO(Al)/CuO(Ni,Al) gradually transitioning from CuO (022) plane with 0.142 nm to NiO (111) plane with 0.241 nm, the energy dispersive spectroscopy (EDS) revealed that the Cu, Ni, and Al elements were distributed uniformly without any evident segregation

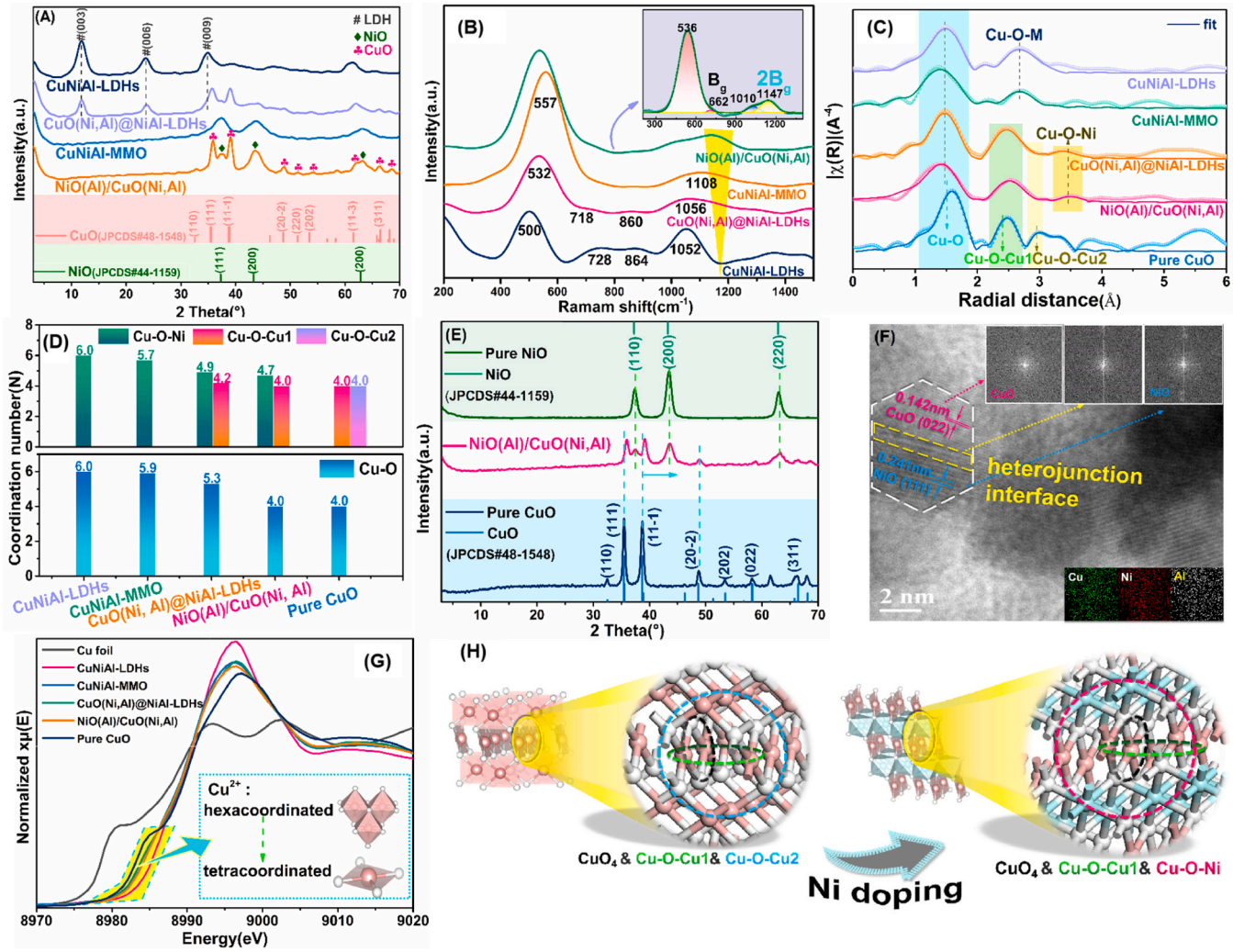

Fig. 1. Structural characterization of IIBH. (A) XRD patterns of CuNiAl-LDHs, CuNiAl-MMO, CuO(Ni,Al)@NiAl-LDHs and NiO(Al)/CuO(Ni,Al). (B) Raman spectra of all photocatalysts by with 532 nm laser excitation and the inset showed the IIBH NiO(Al)/CuO(Ni,Al) multi-peak fitting curve, where the multi-phonon band ($2B_g$) signal can be clearly distinguished. (C) The magnitude of k^3-weighted Fourier transform and corresponding fitting of Cu K-edge XAFS. (D) The EXAFS of fitting results for coordination number of Cu-O, Cu-O-Cu1, Cu-O-Cu2, and Cu-O-Ni shells for all as-prepared samples and the inset is the SEM elemental mapping of Ni, Cu, and Al. (E) XRD patterns of the IIBH NiO(Al)/CuO(Ni,Al), pure CuO and NiO. (F) The HRTEM image of IIBH NiO(Al)/CuO(Ni,Al) and the inset is FFT pattern. (G) The Cu K-edge of XANES and the inset is coordination number of Cu^{2+} gradually changed from $[Cu(OH)_6]$ to $[CuO_4]$ during the whole topological pyrolysis process. (H) Crystalline structural schematic diagram of Ni doped CuO (Nickel: blue; Copper: pink; Oxygen: white). Fitting data and details can be obtained from Tables S3 and S4 in supporting information.

[61]. The inset of Fig. 1F showed that the FFT at the interface includes two different sets of diffraction points of NiO and CuO. It can be speculated that during the two-stage topological pyrolysis process, the CuO (Ni,Al) microphase in-situ formed when the NiAl-LDHs was recovered from the CuNiAl-MMO and the NiO(Al) microphase evolved from the second pyrolysis of NiAl-LDHs, leading to local nucleation of CuO(Ni,Al) and NiO(Al) at the nanometer size, in which the interdiffusion of metal ions enabled by the pyrolysis resulted in intergrowth interface BH, like the known organic BH [62]. This can be considered a successful in-situ construction of IIBH NiO(Al)/CuO(Ni,Al). By comparing the IIBH with pure CuO and NiO (Fig. 1E and Table S2), it is worth noting that the diffraction peaks of CuO in the NiO(Al)/CuO(Ni,Al) moved to a higher angle, which indicated its crystalline lattice contract to some extent due to the smaller Ni^{2+} (r = 69 pm) replaced the bigger Cu^{2+} (r = 73 pm), while those of NiO remained unchanged [63]. Why was not Al^{3+} (r = 54 pm) replacing Cu^{2+}, we did the controlled tests and discussed it in detail in SI (Fig. S4). Similarly, we also observed in the Raman spectra (Fig. 1B) that the signal of Ni^{2+}-doped CuO in the NiO(Al)/CuO(Ni,Al) with the strong multi-phonon band ($2B_g$) at ~1147 cm^{-1} [64]. Since the Raman activity of one phonon band (B_g) is related to the stretching vibration of the atomic orbital d^2_{xy}, the dsp^2 (d^2_{xy}, s, p_x, p_y) hybridized CuO with Ni^{2+} doping affected the electron density in the d^2_{xy} plane, resulting in $2B_g$ band [64]. This transformation in the coordination environment was discussed thoroughly in *R*-space plot from EXAFS. Pure CuO displayed three distinctive peaks (Fig. 1C): the peak at 1.9, 2.8, and 3.1 Å corresponded to the Cu-O, Cu-O-Cu1, and Cu-O-Cu2 shells, respectively [65]. It can be seen that the coordination number of Cu-O and Cu-O-Cu1 shells decreased about 5 for CuO(Ni,Al)@NiAl-LDHs to 4 for NiO (Al)/CuO(Ni,Al), and the Cu-O-Cu2 shell was replaced by the Cu-O-Ni shell at 3.8 Å (Fig. 1D). As we discussed in the supporting information, the Debye-Waller factor (σ^2) is related the crystal disorder, the structure of CuO(Ni,Al) in IIBH distorted from the ideal crystal structure due to Ni^{2+} doping, so the numerical value of σ^2 was somewhat greater (Table S3) and the absorption peak was widened when compared with pure CuO (Fig. 1C) [66]. Additionally, the Ni K-edge absorption sites were almost identical to those of pure NiO, indicating that Ni was in the 2+ oxidation state (Fig. S3). The Ni *R*-space plot in EXAFS revealed that there were primarily two distinctive peaks, in which the ~2.0 and

~2.9 Å peaks represented the Ni-O and Ni-O-Ni shells, respectively [67]. NiO(Al) in IIBH was not significantly different from pure NiO (Table S4), which was completely different that from Cu. Meanwhile, as displayed in Fig. 1G, the Cu K-edge absorption positions of samples in the XAFS were nearly the same as those of pure CuO, suggesting the oxidation state of Cu was 2+. A wide pre-edge peak at ~8985 eV in pure CuO could be observed, which was attributed to the tetra-coordinate geometry of Cu^{2+} [68]. This peak appeared continuously with the topological pyrolysis process, indicating that the coordination of Cu^{2+} gradually changed from the hexa-coordinate structure in the CuNiAl-LDHs to the tetra-coordinated one in the NiO(Al)/CuO (Ni,Al) [68]. We tuned the metal ion content and used ICP-AES to quantify the content of Cu^{2+}, Ni^{2+}, and Al^{3+} in the sample to optimize the CuNiAl-LDHs synthetic ratio to achieve the optimal phase separation between NiO(Al) and CuO (Ni,Al) (Fig. S5 and Table S5). Different calcination temperatures were also explored (Fig. S6), and the difference in structure memory effect between NiAl-LDHs and CuAl-LDHs was also studied (Fig. S7).

As a result of the above, it is clear why the structural memory effect of LDHs might be used to create the IIBH using the TTP method and explained how Ni^{2+} doped CuO. the $[Ni(OH)_6]$, $[Cu(OH)_6]$, or $[Al(OH)_6]$ octahedra shared all of their edges to construct the CuNiAl-LDHs. The Cu^{2+} coordination number progressively altered from $[Cu(OH)_6]$ to $[CuO_4]$ over the whole topological pyrolysis process with dissolution-recrystallization, other than Ni^{2+} remained virtually unchanged. Additionally, ionic diffusion in a solid during pyrolysis is determined by its crystalline structure. The Cu^{2+} ions filled some of the square planar voids in monoclinic CuO, while Ni^{2+} ions filled all of the octahedral voids in cubic NiO. We hypothesize that the remaining octahedral voids in CuO acted as Ni^{2+} diffusion sites. As a consequence, we predict that the Ni^{2+} doping process might be achieved by filling the octahedral voids of CuO, resulting in the Cu-O-Ni shell replacing the Cu-O-Cu2 shell to create a partial substitution solid solution for CuO(Ni,Al) [69–71] (Fig. 1H).

As we know, the outstanding light absorption of photocatalyst was requirements to ensure its high photocatalytic activity [72], so the optical and electrical properties of the photocatalyst were studied.

4.2. Optical and electrochemical performance of photocatalyst

When compared to other catalysts, NiO(Al)/CuO(Ni,Al) displayed superior absorption throughout the whole visible spectral range (Fig. 2A). Furthermore, the maximum absorption in the UV region showed that the band gap of CuNiAl-LDHs was 3.64 eV by using the Kubelka-Munk formula and Tauc's plot (Fig. S8). On the other hand, the absorption from *d-d* transition of Ni^{2+} and Cu^{2+} ions can be found in the visible region. Among these, the $^2E_g \rightarrow {}^2T_{2\,g}$ transition for Cu^{2+} and $^3A_{2\,g} \rightarrow {}^3T_{1\,g}$ transition for Ni^{2+} was at 478 nm and 745 nm, respectively [73]. The light absorption of IIBH retained the characteristics of LDHs while the absorption was enhanced in the whole spectra.

Mott-Schottky experiments were conducted to better define the types of carrier transport for the IIBH. According to the illustration within the inset of Fig. 2B, pure CuO showed a positive slope that was typical of an *n*-type semiconductor and the flat band potential (E_{fb}) of about −0.85 eV (vs Hg/Hg_2Cl_2), while pure NiO had a negative slope that indicated a *p*-type semiconductor and the E_{fb} of about 1.84 eV. Accordingly, the conduction band potential (E_{CB}) of pure CuO was roughly calculated to be −1.15 eV, whereas the valence band potential (E_{VB}) of pure NiO was about 2.04 eV, which was close to the results of the XPS valence band spectra (Fig. S9). There were two linear sections (of the "inverted V" type, Fig. 2B) in the Mott-Schottky plot for the IIBH, and the curve tended to compress inward, which was caused by the electrons flowing from the higher CB of *n*-CuO(Ni,Al) region to the lower one of *p*-NiO(Al) region, until reached to the same Fermi energy value. This was consistent with previous research on identifying *p-n* heterojunction features [74]. Therefore, the as-prepared IIBH can be nominated as the *pn*-IIBH in the following. The photogenerated electron transfer mechanism of *pn*-IIBH NiO(Al)/CuO(Ni,Al) will be discussed later in detail [74–77]. Fig. S10 simultaneously displayed the positive slope of the MS curve for

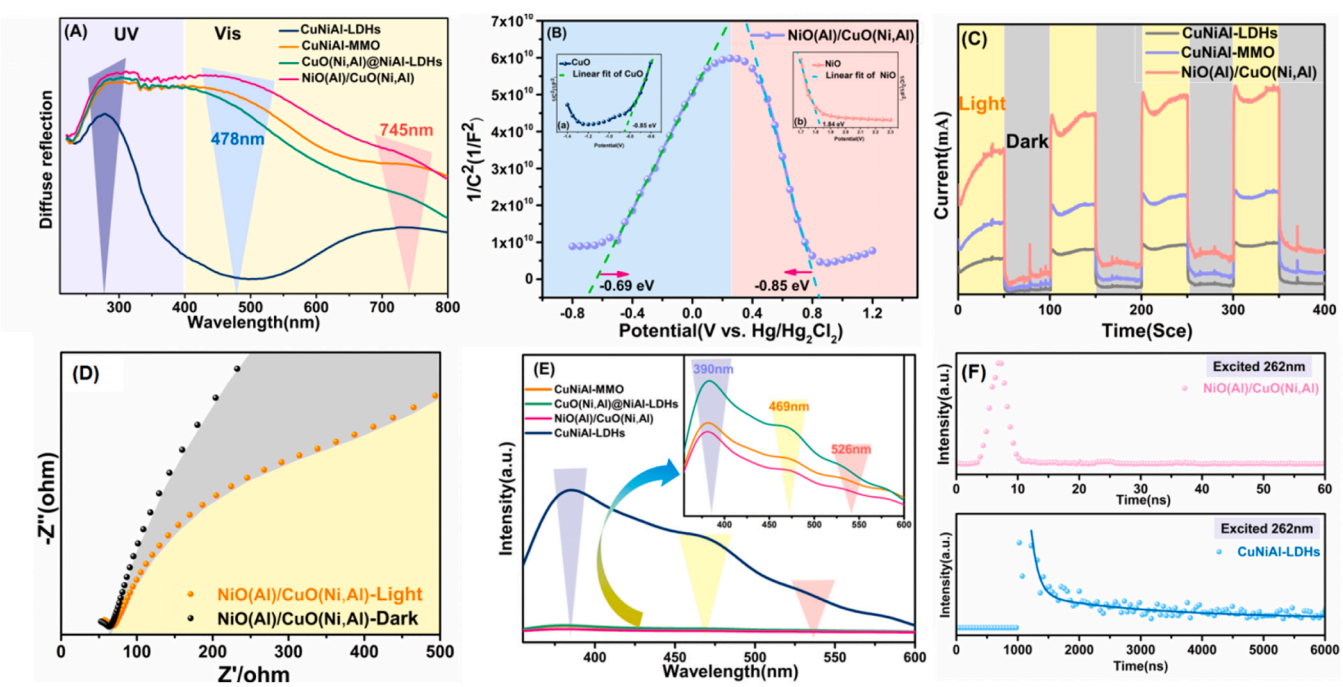

Fig. 2. Optical and electrochemical characteristics of the *pn*-IIBH. (A) UV–Visible diffuse reflectance spectra of CuNiAl-LDHs, CuNiAl-MMO, CuO(Ni,Al)@NiAl-LDHs and NiO(Al)/CuO(Ni,Al). (B) Mott-Schottky plot of the *pn*-IIBH NiO(Al)/CuO(Ni,Al). The left and right inset is that for pure CuO and NiO, respectively. (C) Transient photocurrent response curves of CuNiAl-LDHs, CuNiAl-MMO, and NiO(Al)/CuO(Ni,Al), when the current density was measured with zero applied bias. (D) The EIS of the *pn*-IIBH NiO(Al)/CuO(Ni,Al) in light and dark. (E) The photoluminescece spectra of all catalysts with 320 nm excitation and the inset is the magnified spectra for NiO(Al)/CuO(Ni,Al), CuNiAl-MMO, and CuO(Al)@NiAl-LDHs. (F) TRPL spectra of CuNiAl-LDHs and *pn*-IIBH NiO(Al)/CuO(Ni,Al) with 262 nm excitation and 390 nm emission.

CuNiAl-LDHs, which was a *n*-type semiconductor as well.

Then, the transient photocurrent response of *pn*-IIBH NiO(Al)/CuO(Ni,Al) as shown in Fig. 2C, displayed excellent photocurrent response compared with other samples, which indicated the built-in electric field of *pn*-IIBH can accelerate the directional charge transport effectively. According to the electrochemical impedance spectroscopy (EIS) test, the charge transfer rate was high, in both light and dark (Figs. 2D and S11). Steady-state photoluminescence and time-resolved photoluminescence (PL and TRPL) spectra were obtained to reveal the photogenerated electron-hole combination and migration dynamics. Fig. 2E demonstrated that the major emission peak at 390 nm was caused by the band-band transition combination of photoexcited carriers, the shoulder at 469 nm was generated by the annihilation of free excitons near the energy band edge, and the other shoulder at 526 nm was supplied by bound excitons [78]. The fact that the PL emission intensity of the *pn*-IIBH NiO(Al)/CuO(Ni,Al) was much lower than that of the other samples provided additional proof that the photogenerated radiative combination of carrier was suppressed remarkably. To analyze the fluorescence lifespan and relaxation process of photogenerated exciton, TRPL spectra probed at 262 nm as the excitation wavelength were shown in Fig. 2F. It can be seen that only CuNiAl-LDHs showed fluorescence decay signals, and it lifetime was calculated using multi-exponential fitting [78] (τ_1 = 115.24 ns, τ_2 = 1693.53 ns, and τ_3 = 15,382.16 ns, Table S6). In contrast, the *pn*-IIBH NiO(Al)/CuO(Ni,Al) presented a symmetric pump light signal with almost no detectable fluorescence decay phenomenon, indicating that the *pn*-IIBH made the photogenerated electron-hole pairs separation and accelerated the charge transfer at the heterojunction interface, being consistent with the steady-state PL results. The suitable redox potential, excellent light absorption performance, and efficient photogenerated carrier separation efficiency enable this *pn*-IIBH NiO(Al)/CuO(Ni,Al) competitive potential for photocatalytic reduction of CO_2.

4.3. Photocatalytic performance on CO_2 reduction

We performed an investigation on the photoreduction of CO_2 in an aqueous reaction system under UV–vis light irradiation without sacrificial reagent, to better understand the photocatalytic performance of the *pn*-IIBH NiO(Al)/CuO(Ni,Al). The gaseous products formed were analyzed by gas chromatography. The production analysis showed the typical signals of the final products in the flame ionization detector channel, where signals for O_2, CH_4 and CO were all well-resolved (Fig. S12) and without other products. The main products in the *pn*-IIBH NiO(Al)/CuO(Ni,Al) were methane and oxygen, and their production molar ratio was close to 2:1. Isotope tests further demonstrated the origin of the carbon and hydrogen in the products from CO_2 and H_2O (Fig. S13), indicating that the reaction ($CO_2 + 2H_2O \rightarrow CH_4 + 2O_2$) occurred [16,79,80]. As shown in Fig. 3A-B and Table S8, the *pn*-IIBH NiO(Al)/CuO(Ni,Al) achieved a CH_4 production rate of 86.59 μmol/g·h, which was 4.2 and 1.35 times higher than that of CuNiAl-LDHs (16.31 μmol/g·h) and CuNiAl-MMO (50.85 μmol/g·h), respectively. Meanwhile, the O_2 production rate of NiO(Al)/CuO(Ni,Al) was around 150.84 μmol/g·h. The selectivity of *pn*-IIBH NiO(Al)/CuO(Ni,Al) to CH_4 was up to 87.31% (Fig. 3C), which was superior to those of CuNiAl-LDHs (34.98%) and CuNiAl-MMO (38.31%). It can be seen that NiO(Al)/CuO(Ni,Al) is optimal in terms of photocatalytic efficiency and selectivity, reflecting the need for the construction of *pn*-IIBH. Among all photocatalysts, trace CO can also be detected (Fig. S14A). At the end of the reaction we did not find any generation of liquid-phase products by measuring the NMR hydrogen spectra. The selectivity for methane was analyzed mainly for 2-electron reduction products (CO) and 8-electron reduction products(CH_4). Oxygen quantification becomes a difficult task because of the presence of oxygen in the environment. Generally, it is also possible to determine the oxygen content by quantifying the reaction of oxygen with colorless monovalent copper ammonia ions. However, because the oxygen produced by our photocatalysis was at the micromolar level, the chemical colorimetric method is difficult to use as a standard for its quantification. Therefore, we performed blank and

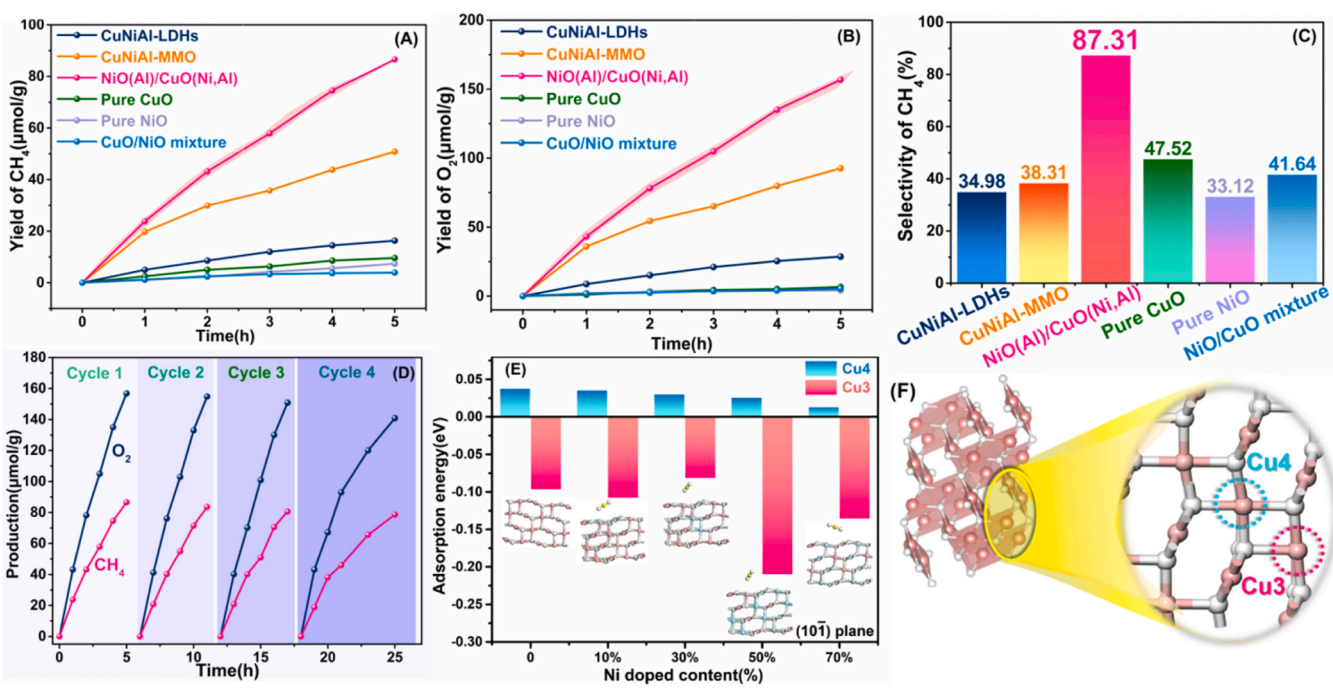

Fig. 3. Photocatalytic performance on CO_2 reduction. (A) The yields of CH_4 for CuNiAl-LDHs, CuNiAl-MMO, NiO(Al)/CuO(Ni,Al), pure CuO, pure NiO, and CuO/NiO mixture. (B) The yields of O_2 of all photocatalysts. (C) CH_4 selectivity of all photocatalysts; (D) The photocatalysis stability of *pn*-IIBH NiO(Al)/CuO(Ni,Al) was studied by 4 photocatalytic cycles. (E) The spin-polarized density functional theory (DFT) calculation of CO_2 adsorption energy on the surface of CuO (10—1) where there are two types of Cu atomic adsorption sites. (F) Atomic adsorption sites schematic diagram toward (10—1) facet of CuO. (The experimental details of photocatalytic reduction CO_2 were provided in supporting information.).

control experiments by performing under the same experimental conditions (Fig. S14B). A control experiment was conducted by utilizing pure CuO, pure NiO, and a CuO/NiO mixture for the photocatalytic reduction of CO_2 to evaluate the production and selectivity. The study revealed that a negligible amount of CH_4 were detected by pure CuO, pure NiO, and CuO/NiO mixture, proving that the compact interface within the *pn*-IIBH NiO(Al)/CuO(Ni,Al) contributed to highly effective methanation. In order to investigate the significance of the presence of Al, some of the Al in the NiO(Al)/CuO(Ni,Al) was etched using alkali (Fig. S16), and a slight decrease in its photocatalytic activity was found (Fig. S17). However, the exact mechanism is still unclear, because only partial etching was performed and the solid-phase reaction could not be fully reacted like the liquid-phase reaction. Finally, after four photocatalytic cycles, the stability of the NiO(Al)/CuO(Ni,Al) was assessed (Fig. 3D). The methane-producing rate did not considerably drop and remained at 90.76%, illustrating that the NiO(Al)/CuO(Ni,Al) were stable and photocorrosion can be neglected during the photocatalytic process. Subsequently, the CO_2 adsorption energy was calculated by density functional theory (DFT), and it was found that there were two types of Cu atomic adsorption sites on the surface of CuO (10—1), namely, tetra-coordinated (Cu4) and tri-coordinated (Cu3). As can be seen from Fig. 3E and F, this tri-coordination unsaturated of Cu^{2+} ions gave stronger adsorption of CO_2, and with the doping of Ni^{2+}, the adsorption energy of CO_2 increased, lowering the activation energy of CO_2 reduction to some extent. In short, compared with the reported *pn* heterojunctions, the *pn*-IIBH NiO(Al)/CuO(Ni,Al) in this paper achieves an advantage in the selectivity and efficiency of CO_2 methanation under UV–vis light (Table S9).

4.4. Photocatalytic mechanism investigations

To explore the high activity and selectivity for CH_4 production over

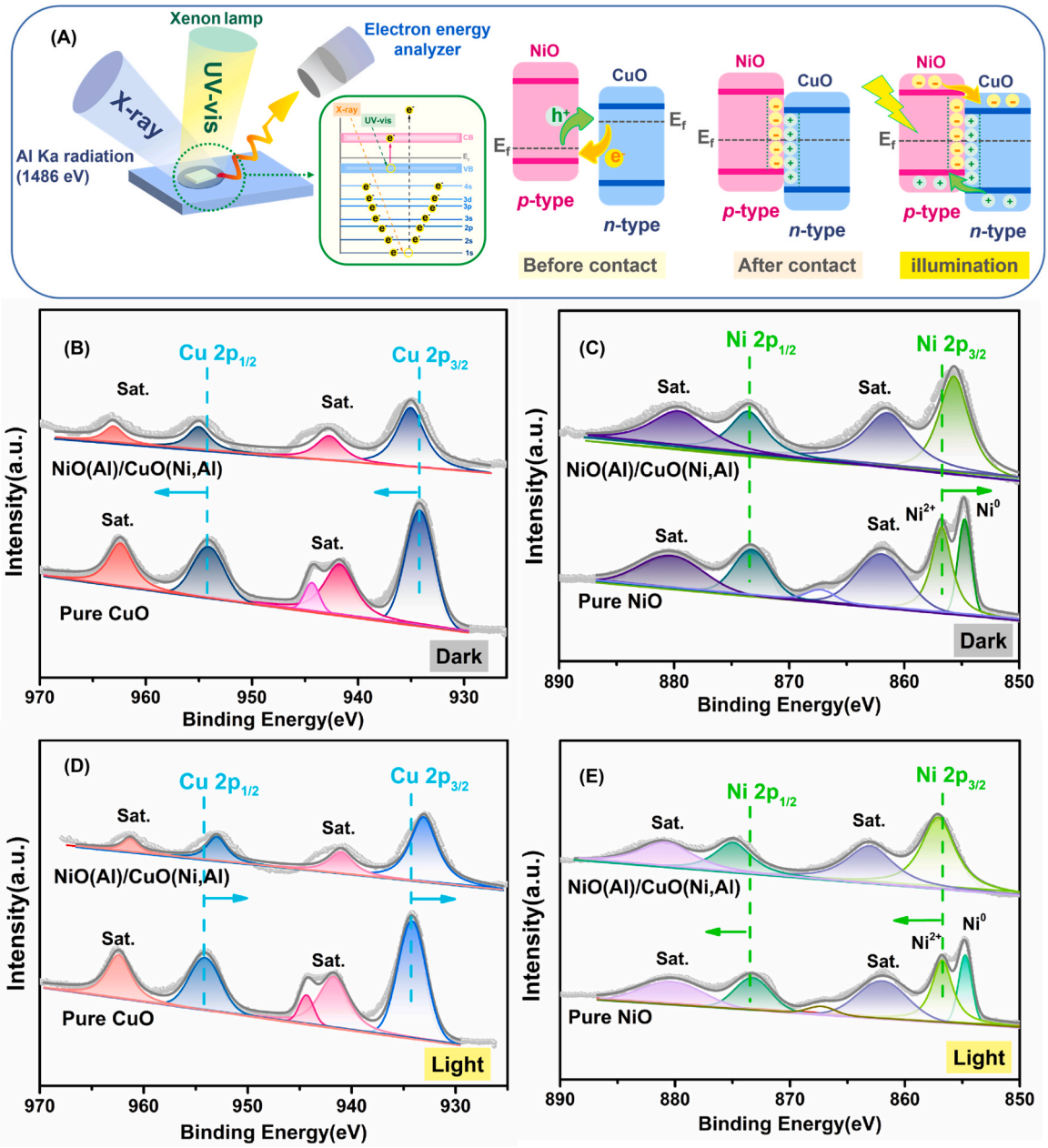

Fig. 4. Photocatalytic mechanism investigation I. (A) ISI-XPS experimental test photo and schematic diagram. XPS spectra of the *pn*-IIBH NiO(Al)/CuO(Ni,Al) and pure CuO, NiO. (B) Cu 2p; (C) Ni 2p. *In-situ* irradiation XPS spectra of the *pn*-IIBH NiO(Al)/CuO(Ni,Al) and pure CuO, NiO. (D) Cu 2p; (E) Ni 2p. (Dark: only using X-ray, Light: using X-ray with UV–vis light.)

the *pn*-IIBH NiO(Al)/CuO(Ni,Al), the photogenerated electron transport and reaction mechanism was investigated. Atoms vary in electron binding energy based on the chemical environment, which reflects changes in electron density. The binding energy decreases with increasing surface electron density. We observed the binding energy shift following photoexcitation using in-situ irradiation X-ray photoelectron spectra (ISI-XPS) (Fig. 4A), which was essential for understanding electron migration [31,81,82]. In Fig. 4B, the Cu $2p_{1/2}$ and Cu $2p_{3/2}$ peaks in XPS, whose binding energies were 934.96 eV and 955.03 eV, respectively, revealed the Cu^{2+} state [83,84] Both the Cu $2p_{1/2}$ and Cu $2p_{3/2}$ peaks moved 0.86 eV to higher binding energy when compared to pure CuO. The binding energies of Ni were 855.67 eV and 873.69 eV for Ni $2p_{3/2}$, Ni $2p_{1/2}$ peaks, respectively, which indicated the presence of Ni^{2+} (Fig. 4C) [85]. In contrast to the Cu 2p peaks mentioned above, the Ni 2p peaks of NiO(Al)/CuO(Ni,Al) shift 1.21 eV to lower binding energy [61]. This suggested that the Fermi energy level (E_f) changed both before and after the formation of the *pn*-IIBH, with electrons moving from the high-E_f *n*-type CuO(Ni,Al) to the low-E_f *p*-type NiO(Al) domains, and an increase in electron density resulting in a decrease in the binding energy. When in-situ illumination was introduced, the binding energy moved in the exact opposite direction from that shown above, indicating that the photogenerated electrons were driven by the built-in electric field, specifically from NiO(Al) and CuO (Ni,Al) domains within the *pn*-IIBH. As a result, the Cu 2p peaks moved to a lower, higher binding energy (Fig. 4D), and the Ni 2p moved to one (Fig. 4E) [63]. The Al 2p and O 1s also showed in Fig. S18A-D, which indicated that Al^{3+} ions doped into both domains. According to Fig. S18E-F, the ISI-XPS of CuNiAl-LDHs was similar to XPS, showing that there was some reason for adopting this technique to illustrate the transfer of photogenerated electrons.

The femtosecond transient absorption spectrum (fs-TAS), which can also record the dynamic scenario of the particle number at each energy level of the excited state with time, may be used to analyze the kinetics and electron transfer process [86,87]. We then performed a series of tests over the *pn*-IIBH NiO(Al)/CuO(Ni,Al) for fs-TAS, with methanol being used as a hole sacrificial agent as a way to probe the photogenerated electron transport [88,89]. The ground state bleach (GSB) at 500 nm with negative optical density (ΔOD) and a wide excited state absorption (ESA) band from 550 nm to 875 nm exhibited in the fs-TAS at different time delays (Fig. 5A) when the *pn*-IIBH NiO(Al)/CuO(Ni,Al) was excited. To identify the origin of these absorption peaks, pure NiO and pure CuO were tested. Under photoexcitation with methanol, the ESA of CuO posited around 590 nm [89] (Fig. 5B), while that of NiO appeared after 650 nm and reached its peak at 780 nm (Fig. 5C). For Cu^{2+} with d^9 ($t_{2g}^6e_g^3$) electronic configuration, there was an absorption peak around 600 nm, corresponding to the $^2E_g \rightarrow {}^2T_{2g}$ transition, while for Ni^{2+} with d^8 ($t_{2g}^6e_g^2$) electronic configuration, its spin-allowed transition $^3A_{2g} \rightarrow {}^3T_{1g}$ absorption was around 800 nm in the infrared region [73]. It was conceivable to suppose that CuO(Ni,Al) domain contributed to the absorption before 650 nm and NiO(Al) one related mostly to the absorption after that in the *pn*-IIBH NiO(Al)/CuO(Ni,Al) [89–91]. As can be observed in Fig. 5D, the ESA band associated with the *d*-orbital of Ni^{2+} continually fell over time from 0.2 ps to 2 ps, whereas that of Cu^{2+} gradually grew, signifying the photogenerated electrons transfer from NiO(Al) domain to CuO(Ni,Al) one, which was consistent with the prior XPS and MS measurement. However, the fs-TAS of CuNiAl-LDHs and CuO/NiO mixture did not show in such obvious dynamic behavior (Fig. S20), demonstrating once again that the *pn*-IIBH NiO(Al)/CuO (Ni, Al) intergrowth interface created by TTP method was the key point to increase photogenerated carrier separation efficiency. The decay curves of *pn*-IIBH NiO(Al)/CuO(Ni,Al) photoelectrons at 590 nm and 780 nm absorption peaks are shown in Fig. 5E. The inset clearly showed that the photoelectron absorption at 780 nm in the NiO(Al) domain decayed immediately after reaching a peak within 2 ps, and then was replaced by a peak at 590 nm in the CuO(Ni,Al) one for a longer decay time within 100 ps. However, pure NiO did not have such the electron transfer pathway, it maintained a long decay at 780 nm and the signal at 590 nm was always negative (Fig. 5F). Although pure CuO displayed approximately the same decay trend at 590 nm and 780 nm, the photogenerated electrons end their lifetime within 40 ps only (Fig. 5G). This extension of the photogenerated electron lifetime created favorable conditions on the *pn*-IIBH NiO(Al)/CuO(Ni,Al), which is favorable for photocatalysis with multiple sequential electron transfer, like the 8-electron reduction process of CO_2 [87].

In order to better understand the photogenerated electron transfer process at the interface of *pn*-IIBH NiO(Al)/CuO(Ni,Al), the differential charge distribution was calculated by spin-polarized density functional theory (DFT) [92]. (*pn*-IIBH modeling details refer to Fig. S21). As shown in Fig. 5H, the red area represented the electron-rich region and the blue one represented the electron-deficient region [93]. It was evident that NiO was primarily surrounded by an electron-deficient region, whereas CuO was mostly surrounded by an electron-rich region. Meanwhile, the work functions of NiO (100) and CuO (10—1) crystalline surfaces were calculated, showing that the work functions of NiO (100) crystalline surfaces were smaller than those of CuO (10—1), satisfying the electron transfer process of the type II heterojunction (Fig. S22). This implied electron migration routes of *pn*-IIBH NiO (Al)/CuO(Ni,Al) was consistent with the above experimental results.

Two known possible pathways for hydrogenation and deoxygenation have been proposed by previous authors for the reaction mechanism of CO_2 methanation, as shown in Fig. 5I [1,86,94–97]. *In-situ* infrared spectra testing was done to keep track of any possible reaction intermediates created when CO_2 and H_2O were introduced into a quartz cell with the *pn*-IIBH and light. The symmetric and antisymmetric stretching vibration of -O-C═O peaks were at 1377 and 1515 cm^{-1}, respectively (Fig. 5J) [33], which increased with irradiation time, demonstrating the existence of the *COOH intermediate [98]. The 3401 and 3603 cm^{-1} peaks attributed to carboxyl hydroxyl and alcohol hydroxyl vibration, respectively. According to the findings, it can be concluded that the *pn*-IIBH NiO(Al)/CuO(Ni,Al) could speed up charge transfer and increase the capacity of H_2O oxidation. This allowed for the quick generation of protons, which then reacted with the adsorbed CO_2 to produce *COOH intermediates. Based on the examination of the pertinent intermediates, it can be said that *pn*-IIBH NiO(Al)/CuO(Ni,Al) primarily employed the hydrogenation pathway rather than the deoxygenation route to perform CO_2 methanation. The group vibration peaks for details were summarized in Table S10. However, the intermediates of *COOH were not found at all for CuNiAl-LDHs (Fig. S23B), instead, only the faint adsorption vibration peak of CO_2 (2360 cm^{-1}).

The photocatalytic mechanism of CO_2 methanation by the *pn*-IIBH NiO(Al)/CuO(Ni,Al) was postulated in accordance with the above-mentioned experimental results, as depicted in Scheme 2. The electrons in the valence band (VB) of the *p*-NiO(Al) (1.64 eV) and *n*-CuO(Ni, Al) (2.04 eV) within the *pn*-IIBH were activated by illumination and subsequently transferred to their conducting band (CB) (−1.71 eV and −1.05 eV, respectively). Additionally, photogenerated carries directed migrated at the intergrowth interface of *pn*-IIBH NiO(Al)/CuO(Ni,Al), which allowed long-lived photogenerated electrons to accumulate on the CuO(Ni,Al) side. Finally, four consecutive hydrogenation steps (HCOOH, HCHO, CH_3OH) on CuO(Ni,Al) domain converted a CO_2 into a CH_4. Each reaction was made up of two proton-electron elementary reactions. Only electron transfer that created the adsorbed [HCOOH] was what determine the average rate of reaction [76]. According to the XRD of the NiO(Al)/CuO(Ni,Al) before and after the photocatalytic reaction (Fig. S24), the crystalline structure remained impacted and no new phase generated, but the XPS displayed that part of Cu^{2+} changed to Cu^+ and Ni^{2+} changed to Ni^{3+} after the reaction (Fig. S25). The redox couple (Cu^{2+}/Cu^+ and Ni^{3+}/Ni^{2+}) was used for electrons and holes transport. Therefore, we made the assumption that photogenerated electrons conveyed to CB of CuO(Ni,Al) to be reduced to Cu^+ momentarily, after which electrons were given to CO_2 for reduction and Cu^+ immediately returned to Cu^{2+}, continuing the cycle. One possible

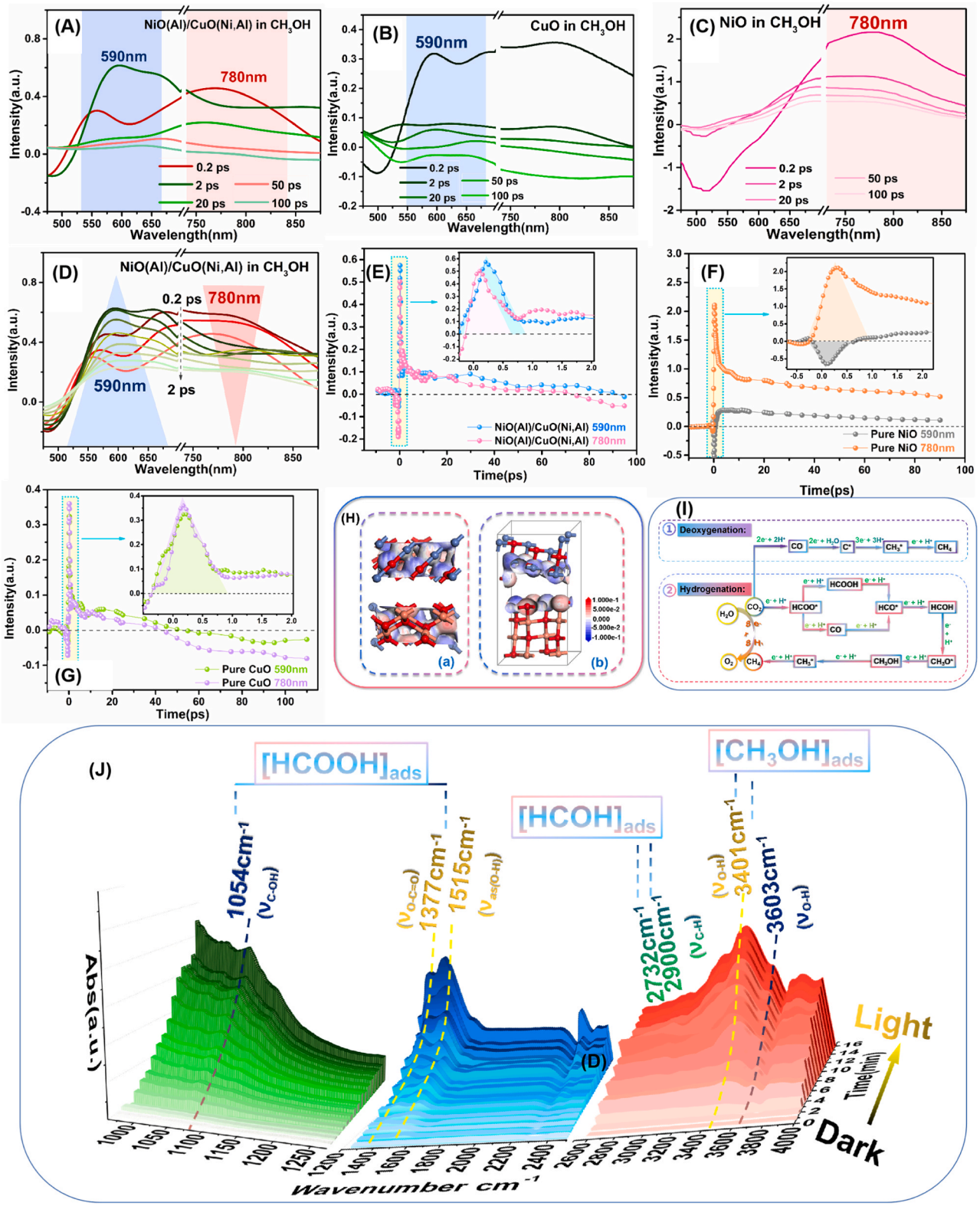

Fig. 5. Photocatalytic mechanism investigation II. Femtosecond transient absorption spectra (fs-TAS) of (A) NiO(Al)/CuO(Ni,Al), (B) pure CuO and (C) pure NiO recorded with 360 nm excitation in CH_3OH. (D) fs-TAS of NiO(Al)/CuO(Ni,Al) between 0.2 ps and 2 ps with 360 nm excitation in CH_3OH. The decay curves at 590 nm and 780 nm in CH_3OH within 100 ps of (E) NiO(Al)/CuO(Ni,Al), (F) pure NiO, and (G) pure CuO and the inset was a large part of the enlargement in 2 ps. (H) The differential charge distribution of the *pn*-IIBH NiO/CuO(Ni) and calculation of specific information refer to the supporting information. (a) top view; (b) side view. (I) Two possible pathways for photocatalytic CO_2 methanation. (J) *In-situ* FTIR of the *pn*-IIBH NiO(Al)/CuO(Ni,Al). Blank background was collected at room temperature, and then high-pure CO_2 and water vapor were into the in-situ spectroscopic cell by the bubbling-method. The spectra were collected at an interval of 2 min and continued to be irradiated for 20 min to obtain the spectra of CO_2 with the various illumination time. (The 2D plots view of the in-situ IR is placed in the SI to also visualize the changes in the intermediate products).

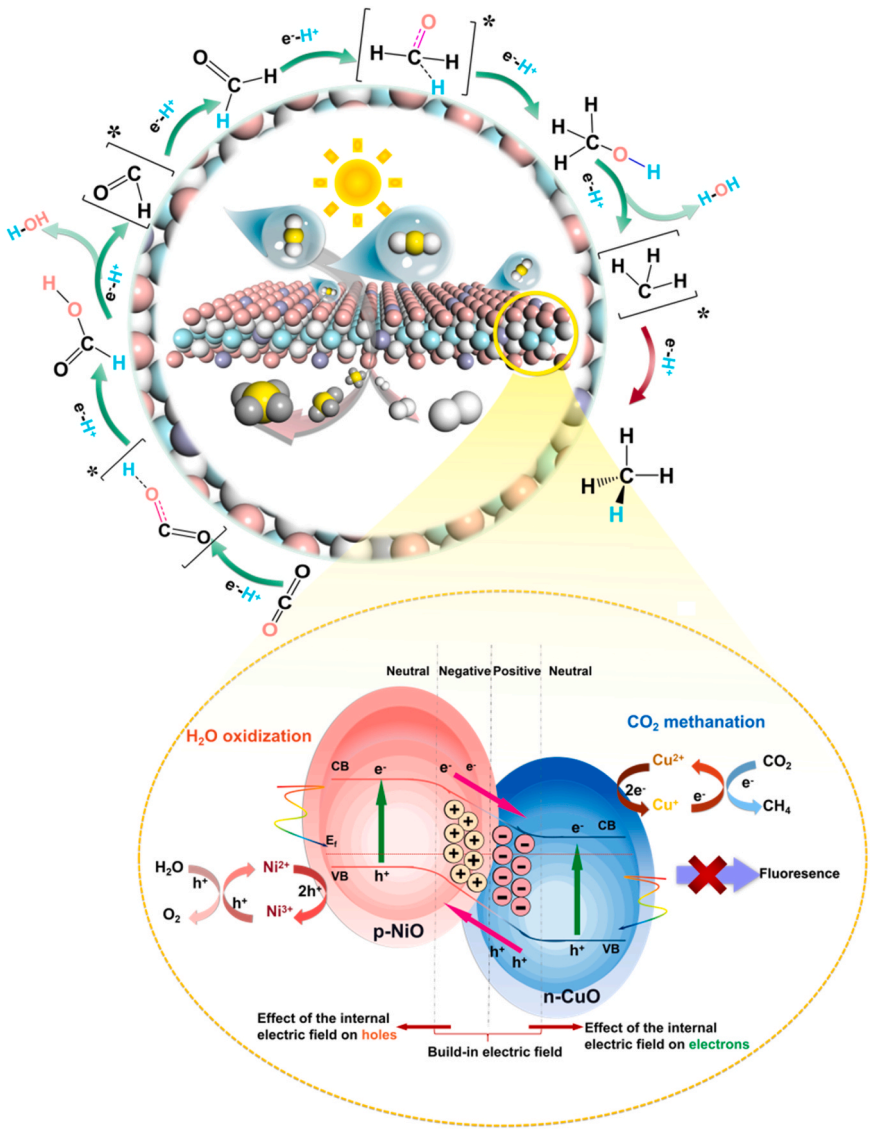

Scheme 2. The CO_2 methanation reaction mechanism of *pn*-IIBH NiO(Al)/CuO(Ni,Al) and established build-in electric field to accelerate photogenerated electron-hole pairs separation.

situation here was that if the photogenerated electrons accumulated on the surface of CuO(Ni,Al) might lead to its reduction by Cu_2O, which was what we refer to as photocorrosion of the catalyst. However, the previous photocatalytic cycle stability and the above experimental results can prove that the *pn*-IIBH NiO(Al)/CuO(Ni,Al) can maintain high stability and activity in photocatalysis. The reasons can be summarized as follows: 1) the built-in electric field of the *pn*-IIBH accelerated the directional charge transport to optimize the carrier migration path; 2) the dense intergrowth interface of the *pn*-IIBH reduced the carrier diffusion length towards the reaction active site; 3) the CO_2 adsorption energy on the CuO(Ni,Al) domain increased by the Ni-doped; and 4) the CO_2 reduction was coupled with the H_2O oxidation, and the methanation was realized at the active sites of CuO(Ni,Al) domain in the *pn*-IIBH.

5. Conclusions

Based on the unique structural memory effect of CuNiAl-LDHs, the two-stage topological pyrolysis (TTP) method was developed to construct the *pn*-IIBH: NiO(Al)/CuO(Ni,Al). We attempted to demonstrate the electron transfer process and thus attribute the heterojunction type using Mott-Schottky curves, in-situ irradiation X-ray photoelectron spectra, femtosecond transient absorption spectra and DFT calculations. Structural characterizations demonstrated that this topological transformation enabled the interface of bulk heterojunction to exist in an intergrowth state, reducing the recombination of photogenerated electron-hole pairs and shortening the electron diffusion distance towards the reaction sites. This allowed photogenerated electrons to accumulate on the CuO(Ni,Al) domain in the *pn*-IIBH, enabling the 8-electron reduction of CO_2 for methanation. Additionally, during the topological transformation process, the different crystalline domains of NiO(Al) and CuO(Ni,Al) led to different diffusion paths for Cu^{2+} and Ni^{2+} which can be regarded as a novel approach for inorganic bulk heterojunction, allowing for the creation of Ni-doped CuO. DFT calculations displayed that this facilitated CO_2 adsorption on the CuO(Ni,Al) domain. Hence, without the sacrifice reagent, stoichiometric photocatalytic methanation for CO_2 and H_2O was realized by the *pn*-IIBH NiO(Al)/CuO(Ni,Al) and the yield and selectivity of CH_4 were 86.59 μmol/g·h, 87.31% and 4.2 times that of CuNiAl-LDHs and 1.35 times that of CuNiAl-MMO, and the reaction, $CO_2 + 2H_2O \rightarrow CH_4 + 2O_2$, was realized indeed. This study illustrates how this particular *pn*-IIBH helps to enhance the photocatalytic CO_2 methanation aimed to artificial photosynthesis and it is confirmed that this *pn*-IIBH paves a novel way for the

photocatalyst design and applications.

CRediT authorship contribution statement

Yuexian Li: Material synthesis, Data curation, Formal analysis, Software, Writing – original draft. **Wenli Su:** Data curation, Writing – original draft. **Yusen Yang:** Data processing. **Lianxia Bai:** Data curation. **Jun Lu:** Theoretical direction, Conceptualization, Funding acquisition, Writing – review & editing. **Wenkai Zhang:** Visualization, Writing – review & editing. **Shuo Wei:** Validation, Writing – review & editing.

Declaration of Competing Interest

The authors declare that they have no known competing financial interests or personal relationships that could have appeared to influence the work reported in this paper.

Data availability

No data was used for the research described in the article.

Acknowledgments

This work was financially supported by the 973 Program (Grant No.: 2014CB932101), the National Natural Science Foundation of China, 111 Project (Grant No.: B07004), Program for Changjiang Scholars and Innovative Research Team in University (IRT1205), and the Fundamental Research Funds for the Central Universities (buctrc201527).

Appendix A. Supporting information

Supplementary data associated with this article can be found in the online version at doi:10.1016/j.apcatb.2023.123282.

References

[1] P. Frontera, A. Macario, M. Ferraro, P. Antonucci, Supported catalysts for CO_2 methanation: a review, Catalysts 7 (2017) 59, https://doi.org/10.3390/catal7020059.
[2] S. Li, L. Gao, Greenhouse gas emissions from synthetic natural gas production, Nat. Clim. Change 6 (2016) 220–221, https://doi.org/10.1038/nclimate2887.
[3] V.M. Lebarbier, R.A. Dagle, L. Kovarik, K.O. Albrecht, X. Li, L. Li, C.E. Taylor, X. Bao, Y. Wang, Sorption-enhanced synthetic natural gas (SNG) production from syngas: a novel process combining CO methanation, water-gas shift, and CO_2 capture, Appl. Catal. B Environ. 144 (2014) 223–232, https://doi.org/10.1016/j.apcatb.2013.06.034.
[4] G.B. Bodedla, Y. Dong, G. Tang, J. Zhao, F. Zhang, X. Zhu, W.-Y. Wong, Long-lived excited states of platinum(ii)-porphyrins for highly efficient photocatalytic hydrogen evolution, J. Mater. Chem. A 10 (2022) 13402–13409, https://doi.org/10.1039/D2TA02543D.
[5] U. Ulmer, T. Dingle, P.N. Duchesne, R.H. Morris, A. Tavasoli, T. Wood, G.A. Ozin, Fundamentals and applications of photocatalytic CO_2 methanation, Nat. Commun. 10 (2019), 3169, https://doi.org/10.1038/s41467-019-10996-2.
[6] R.-P. Ye, L. Liao, T.R. Reina, J. Liu, D. Chevella, Y. Jin, M. Fan, J. Liu, Engineering Ni/SiO_2 catalysts for enhanced CO_2 methanation, Fuel 285 (2021), 119151, https://doi.org/10.1016/j.fuel.2020.119151.
[7] A. Loder, M. Siebenhofer, S. Lux, The reaction kinetics of CO_2 methanation on a bifunctional Ni/MgO catalyst, J. Ind. Eng. Chem. 85 (2020) 196–207, https://doi.org/10.1016/j.jiec.2020.02.001.
[8] Y. Wang, X. Shang, J. Shen, Z. Zhang, D. Wang, J. Lin, J.C.S. Wu, X. Fu, X. Wang, C. Li, Direct and indirect Z-scheme heterostructure-coupled photosystem enabling cooperation of CO_2 reduction and H_2O oxidation, Nat. Commun. 11 (2020), 3043, https://doi.org/10.1038/s41467-020-16742-3.
[9] S. Sundaram, C. Diehl, N.S. Cortina, J. Bamberger, N. Paczia, T.J. Erb, Inside cover: a modular invitro platform for the production of terpenes and polyketides from CO_2, Angew. Chem. Int. Ed. 60 (2021), https://doi.org/10.1002/anie.202106778.
[10] Y. Feng, C. Wang, P. Cui, C. Li, B. Zhang, L. Gan, S. Zhang, X. Zhang, X. Zhou, Z. Sun, K. Wang, Y. Duan, H. Li, K. Zhou, H. Huang, A. Li, C. Zhuang, L. Wang, Z. Zhang, X. Han, Ultrahigh photocatalytic CO_2 reduction efficiency and selectivity manipulation by single-tungsten-atom oxide at the atomic step of TiO_2, Adv. Mater. 34 (2022), 2109074, https://doi.org/10.1002/adma.202109074.
[11] S. Jayachitra, D. Mahendiran, P. Ravi, P. Murugan, M. Sathish, Highly conductive $NiSe_2$ nanoparticle as a co-catalyst over TiO_2 for enhanced photocatalytic hydrogen production, Appl. Catal. B Environ. 307 (2022), 121159, https://doi.org/10.1016/j.apcatb.2022.121159.
[12] K.M. Kamal, R. Narayan, N. Chandran, S. Popović, M.A. Nazrulla, J. Kovač, N. Vrtovec, M. Bele, N. Hodnik, M.M. Kržmanc, B. Likozar, Synergistic enhancement of photocatalytic CO_2 reduction by plasmonic Au nanoparticles on TiO_2 decorated N-graphene heterostructure catalyst for high selectivity methane production, Appl. Catal. B Environ. 307 (2022), 121181, https://doi.org/10.1016/j.apcatb.2022.121181.
[13] P. Madhusudan, R. Shi, S. Xiang, M. Jin, B.N. Chandrashekar, J. Wang, W. Wang, O. Peng, A. Amini, C. Cheng, Construction of highly efficient Z-scheme $Zn_xCd_{1-x}S$/Au@g-C_3N_4 ternary heterojunction composite for visible-light-driven photocatalytic reduction of CO_2 to solar fuel, Appl. Catal. B Environ. 282 (2021), 119600, https://doi.org/10.1016/j.
[14] P. Liu, Z. Huang, X. Gao, X. Hong, J. Zhu, G. Wang, Y. Wu, J. Zeng, X. Zheng, Synergy between palladium single atoms and nanoparticles via hydrogen spillover for enhancing CO_2 photoreduction to CH_4, Adv. Mater. 34 (2022), 2200057, https://doi.org/10.1002/adma.202200057.
[15] X.-Q. Tan, S.-F. Ng, A.R. Mohamed, W.-J. Ong, Point-to-face contact heterojunctions: Interfacial design of 0D nanomaterials on 2D g-C_3N_4 towards photocatalytic energy applications, Carbon Energy 4 (2022) 665–730, https://doi.org/10.1002/cey2.252.
[16] Y. Wang, Z. Zhang, L. Zhang, Z. Luo, J. Shen, H. Lin, J. Long, J.C.S. Wu, X. Fu, X. Wang, C. Li, Visible-light driven overall conversion of CO_2 and H_2O to CH_4 and O_2 on 3D-SiC@2D-MoS_2 heterostructure, J. Am. Chem. Soc. 140 (2018) 14595–14598, https://doi.org/10.1021/jacs.8b09344.
[17] H. Dau, E. Fujita, L. Sun, Artificial photosynthesis: beyond mimicking nature, ChemSusChem 10 (2017) 4228–4235, https://doi.org/10.1002/cssc.201702106.
[18] S. Ye, C. Ding, M. Liu, A. Wang, Q. Huang, C. Li, Water oxidation catalysts for artificial photosynthesis, Adv. Mater. 31 (2019), 1902069, https://doi.org/10.1002/adma.201902069.
[19] B. Qiu, M. Du, Y. Ma, Q. Zhu, M. Xing, J. Zhang, Integration of redox cocatalysts for artificial photosynthesis, Energy Environ. Sci. 14 (2021) 5260–5288, https://doi.org/10.1039/D1EE02359D.
[20] S. Lee, G.Y. Jang, J.K. Kim, J.H. Park, Solar-harvesting lead halide perovskite for artificial photosynthesis, J. Energy Chem. 62 (2021) 11–26, https://doi.org/10.1016/j.jechem.2021.02.025.
[21] L. Che, J. Pan, K. Cai, Y. Cong, S.-W. Lv, The construction of p-n heterojunction for enhancing photocatalytic performance in environmental application: a review, Sep. Purif. Technol. 315 (2023), 123708, https://doi.org/10.1016/j.seppur.2023.123708.
[22] M.-Z. Qin, W.-X. Fu, H. Guo, C.-G. Niu, D.-W. Huang, C. Liang, Y.-Y. Yang, H.-Y. Liu, N. Tang, Q.-Q. Fan, 2D/2D Heterojunction systems for the removal of organic pollutants: a review, Adv. Colloid Interface Sci. 297 (2021), 102540, https://doi.org/10.1016/j.cis.2021.102540.
[23] Y. Yuan, R.-t Guo, L.-f Hong, X.-y Ji, Z.-d Lin, Z.-s Li, W.-g Pan, A review of metal oxide-based Z-scheme heterojunction photocatalysts: actualities and developments, Mater. Today Energy 21 (2021), 100829, https://doi.org/10.1016/j.mtener.2021.100829.
[24] A. Kumar, A. Khosla, S. Kumar Sharma, P. Dhiman, G. Sharma, L. Gnanasekaran, M. Naushad, F.J. Stadler, A review on S-scheme and dual S-scheme heterojunctions for photocatalytic hydrogen evolution, water detoxification and CO_2 reduction, Fuel 333 (2023), 126267, https://doi.org/10.1016/j.fuel.2022.126267.
[25] M. Edelmannová, K.-Y. Lin, J.C.S. Wu, I. Troppová, L. Čapek, K. Kočí, Photocatalytic hydrogenation and reduction of CO_2 over CuO/ TiO_2 photocatalysts, Appl. Surf. Sci. 454 (2018) 313–318, https://doi.org/10.1016/j.apsusc.2018.05.123.
[26] E. Morais, C. O'Modhrain, K.R. Thampi, J.A. Sullivan, RuO_2/TiO_2 photocatalysts prepared via a hydrothermal route: Influence of the presence of TiO_2 on the reactivity of RuO_2 in the artificial photosynthesis reaction, J. Catal. 401 (2021) 288–296, https://doi.org/10.1016/j.jcat.2021.08.007.
[27] M. Tahir, B. Tahir, N.A.S. Amin, A. Muhammad, Photocatalytic CO_2 methanation over NiO/In_2O_3 promoted TiO_2 nanocatalysts using H_2O and/or H_2 reductants, Energy Convers. Manag. 119 (2016) 368–378, https://doi.org/10.1016/j.enconman.2016.04.057.
[28] X. Han, B. Lu, X. Huang, C. Liu, S. Chen, J. Chen, Z. Zeng, S. Deng, J. Wang, Novel p- and n-type S-scheme heterojunction photocatalyst for boosted CO_2 photoreduction activity, Appl. Catal. B Environ. 316 (2022), 121587, https://doi.org/10.1016/j.apcatb.2022.121587.
[29] Z. Tang, W. He, Y. Wang, Y. Wei, X. Yu, J. Xiong, X. Wang, X. Zhang, Z. Zhao, J. Liu, Ternary heterojunction in rGO-coated Ag/Cu_2O catalysts for boosting selective photocatalytic CO_2 reduction into CH_4, Appl. Catal. B Environ. 311 (2022), 121371, https://doi.org/10.1016/j.apcatb.2022.121371.
[30] H. Peng, X. Deng, G. Li, Q. Wang, M. Song, P. Chen, S.-F. Yin, Oxygen vacancy and Van der Waals heterojunction modulated interfacial chemical bond over Mo_2C/$Bi_4O_5Br_2$ for boosting photocatalytic CO_2 reduction, Appl. Catal. B Environ. 318 (2022), 121866, https://doi.org/10.1016/j.apcatb.2022.121866.
[31] M. Yang, P. Wang, Y. Li, S. Tang, X. Lin, H. Zhang, Z. Zhu, F. Chen, Graphene aerogel-based NiAl-LDH/g-C_3N_4 with ultratight sheet-sheet heterojunction for excellent visible-light photocatalytic activity of CO_2 reduction, Appl. Catal. B Environ. 306 (2022), 121065, https://doi.org/10.1016/j.apcatb.2022.121065.
[32] W. He, L. Liu, T. Ma, H. Han, J. Zhu, Y. Liu, Z. Fang, Z. Yang, K. Guo, Controllable morphology $CoFe_2O_4$/g-C_3N_4 p-n heterojunction photocatalysts with built-in electric field enhance photocatalytic performance, Appl. Catal. B Environ. 306 (2022), 121107, https://doi.org/10.1016/j.apcatb.2022.121107.
[33] J. Jiang, X. Wang, Q. Xu, Z. Mei, L. Duan, H. Guo, Understanding dual-vacancy heterojunction for boosting photocatalytic CO_2 reduction with highly selective

conversion to CH_4, Appl. Catal. B Environ. 316 (2022), 121679, https://doi.org/10.1016/j.apcatb.2022.121679.
[34] R. Ren, G. Liu, J.Y. Kim, R.E.A. Ardhi, M.X. Tran, W. Yang, J.K. Lee, Photoactive g-C_3N_4/CuZIF-67 bifunctional electrocatalyst with staggered p-n heterojunction for rechargeable Zn-air batteries, Appl. Catal. B Environ. 306 (2022), 121096, https://doi.org/10.1016/j.apcatb.2022.121096.
[35] A.R. Jadhav, V.Q. Bui, Y. Cho, Y. Liu, A. Kumar, H. Kim, S. Ajmal, X. Liu, S. Saqlain, J. Lee, H. Kim, Y.D. Kim, S.-G. Kim, H. Lee, Unveiling a three phase mixed heterojunction via phase-selective anchoring of polymer for efficient photocatalysis, Adv. Energy Mater. 12 (2022), 2102116, https://doi.org/10.1002/aenm.202102116.
[36] J. Ding, S. Fu, K. Hu, G. Zhang, M. Liu, X. Zhang, R. Wang, X. Qiu, Efficient hot electron capture in CuPc/$MoSe_2$ heterostructure assisted by intersystem crossing, Nano Lett. 22 (2022) 8463–8469, https://doi.org/10.1021/acs.nanolett.2c02748.
[37] J. Kosco, S. Gonzalez-Carrero, C.T. Howells, T. Fei, Y. Dong, R. Sougrat, G. T. Harrison, Y. Firdaus, R. Sheelamanthula, B. Purushothaman, F. Moruzzi, W. Xu, L. Zhao, A. Basu, S. De Wolf, T.D. Anthopoulos, J.R. Durrant, I. McCulloch, Generation of long-lived charges in organic semiconductor heterojunction nanoparticles for efficient photocatalytic hydrogen evolution, Nat. Energy 7 (2022) 340–351, https://doi.org/10.1038/s41560-022-00990-2.
[38] X. Sun, Z. Shao, Z. Li, D. Liu, C. Gao, C. Chen, B. Zhang, L. Hao, Q. Zhao, Y. Li, X. Wang, Y. Lu, X. Wang, G. Cui, S. Pang, Highly efficient $CsPbI_3/Cs_{1-x}DMA_xPbI_3$ bulk heterojunction perovskite solar cell, Joule 6 (2022) 850–860, https://doi.org/10.1016/j.joule.2022.02.004.
[39] W. Gao, F. Qi, Z. Peng, F.R. Lin, K. Jiang, C. Zhong, W. Kaminsky, Z. Guan, C.-S. Lee, T.J. Marks, H. Ade, A.K.Y. Jen, Achieving 19% power conversion efficiency in planar-mixed heterojunction organic solar cells using a pseudosymmetric electron acceptor, Adv. Mater. 34 (2022), 2202089, https://doi.org/10.1002/adma.202202089.
[40] G. Yu, J. Gao, J.C. Hummelen, F. Wudl, A.J. Heeger, Polymer photovoltaic cells: enhanced efficiencies via a network of internal donor-acceptor heterojunctions, Science 270 (1995) 1789–1791, https://doi.org/10.1126/science.270.5243.1789.
[41] N.S. Sariciftci, L. Smilowitz, A.J. Heeger, F. Wudl, Photoinduced electron transfer from a conducting polymer to buckminsterfullerene, Science 258 (1992) 1474–1476, https://doi.org/10.1126/science.258.5087.1474.
[42] X. Li, W. Zhang, X. Guo, C. Lu, J. Wei, J. Fang, Constructing heterojunctions by surface sulfidation for efficient inverted perovskite solar cells, Science 375 (2022) 434–437, https://doi.org/10.1126/science.abl5676.
[43] R. Azmi, E. Ugur, A. Seitkhan, F. Aljamaan, A.S. Subbiah, J. Liu, G.T. Harrison, M. I. Nugraha, M.K. Eswaran, M. Babics, Y. Chen, F. Xu, T.G. Allen, Au Rehman, C.-L. Wang, T.D. Anthopoulos, U. Schwingenschlögl, M. De Bastiani, E. Aydin, S. De Wolf, Damp heat–stable perovskite solar cells with tailored-dimensionality 2D/3D heterojunctions, Science 376 (2022) 73–77, https://doi.org/10.1126/science.abm5784.
[44] X. Xu, L. Yu, H. Meng, L. Dai, H. Yan, R. Li, Q. Peng, Polymer solar cells with 18.74% efficiency: from bulk heterojunction to interdigitated bulk heterojunction, Adv. Funct. Mater. 32 (2022), 2108797, https://doi.org/10.1002/adfm.202108797.
[45] J.W. Mok, Z. Hu, C. Sun, I. Barth, R. Muñoz, J. Jackson, T. Terlier, K.G. Yager, R. Verduzco, Network-stabilized bulk heterojunction organic photovoltaics, Chem. Mater. 30 (2018) 8314–8321, https://doi.org/10.1021/acs.chemmater.8b03791.
[46] J. Song, M. Zhang, M. Yuan, Y. Qian, Y. Sun, F. Liu, Morphology characterization of bulk heterojunction solar cells, Small Methods 2 (2018), 1700229, https://doi.org/10.1002/smtd.201700229.
[47] A. Wadsworth, Z. Hamid, J. Kosco, N. Gasparini, I. McCulloch, The bulk heterojunction in organic photovoltaic, photodetector, and photocatalytic applications, Adv. Mater. 32 (2020), 2001763, https://doi.org/10.1002/adma.202001763.
[48] S. Kumaravel, K. Karthick, S.S. Sankar, A. Karmakar, R. Madhu, K. Bera, S. Kundu, Current progressions in transition metal based hydroxides as bi-functional catalysts towards electrocatalytic total water splitting, Sustain. Energy Fuels 5 (2021) 6215–6268, https://doi.org/10.1039/D1SE01193F.
[49] J. Feng, Y. He, Y. Liu, Y. Du, D. Li, Supported catalysts based on layered double hydroxides for catalytic oxidation and hydrogenation: general functionality and promising application prospects, Chem. Soc. Rev. 44 (2015) 5291–5319, https://doi.org/10.1039/C5CS00268K.
[50] H.W.P. Carvalho, S.H. Pulcinelli, C.V. Santilli, F. Leroux, F. Meneau, V. Briois, XAS/WAXS time-resolved phase speciation of chlorine LDH thermal transformation: emerging roles of isovalent metal substitution, Chem. Mater. 25 (2013) 2855–2867, https://doi.org/10.1021/cm401352t.
[51] Q. Meng, H. Yan, Theoretical study on the topotactic transformation and memory effect of M (II) M (III)-layered double hydroxides, Mol. Simul. 43 (2017) 1338–1347, https://doi.org/10.1080/08927022.2017.1362107.
[52] X. Zheng, D. Liu, J. Wen, S. Lv, Nonthermal plasma-vulcanized flower-like ZnS/Zn-Al composites from Zn-Al layered double hydroxides for the adsorption-photo-reduction of Cr(VI), Sep. Purif. Technol. 275 (2021), 117934, https://doi.org/10.1016/j.seppur.2020.117934.
[53] E.M. Seftel, M. Puscasu, M. Mertens, P. Cool, G. Carja, Photo-responsive behavior of γ-Fe_2O_3 NPs embedded into ZnAlFe-LDH matrices and their catalytic efficiency in wastewater remediation, Catal. Today 252 (2015) 7–13, https://doi.org/10.1016/j.cattod.2014.11.039.
[54] Z. Zheng, D. Wu, G. Chen, N. Zhang, H. Wan, X. Liu, R. Ma, Microcrystallization and lattice contraction of NiFe LDHs for enhancing water electrocatalytic oxidation, Carbon Energy 4 (2022) 901–913, https://doi.org/10.1002/cey2.215.
[55] Y. Wang, S. Wang, Z.-L. Ma, L.-T. Yan, X.-B. Zhao, Y.-Y. Xue, J.-M. Huo, X. Yuan, S.-N. Li, Q.-G. Zhai, Competitive coordination-oriented monodispersed ruthenium sites in conductive MOF/LDH hetero-nanotree catalysts for efficient overall water splitting in alkaline media, Adv. Mater. 34 (2022), 2107488, https://doi.org/10.1002/adma.202107488.
[56] Y. Wu, Y. Gong, J. Liu, T. Chen, Q. Liu, Y. Zhu, L. Niu, C. Li, X. Liu, C.Q. Sun, S. Xu, Constructing NiFe-LDH wrapped Cu_2O nanocube heterostructure photocatalysts for enhanced photocatalytic dye degradation and CO_2 reduction via Z-scheme mechanism, J. Alloy. Compd. 831 (2020), 154723, https://doi.org/10.1016/j.jallcom.2020.154723.
[57] X. Yang, H. Zhang, W. Xu, B. Yu, Y. Liu, Z. Wu, A doping element improving the properties of catalysis: in situ Raman spectroscopy insights into Mn-doped NiMn layered double hydroxide for the urea oxidation reaction, Catal. Sci. Technol. 12 (2022) 4471–4485, https://doi.org/10.1039/D2CY00308B.
[58] W.R.K. Thalgaspitiya, T.K. Kapuge, D. Rathnayake, J. He, W.S. Willis, S.L. Suib, A novel generalized metal dissolution approach for the synthesis of mixed valent mesoporous metal oxides, Mater. Today 35 (2020) 50–68, https://doi.org/10.1016/j.mattod.2019.10.024.
[59] D. Wu, F. He, Y. Dai, Y. Xie, Y. Ling, L. Liu, J. Zhao, H. Ye, Y. Hou, A heterostructured ZnAl-LDH@ZIF-8 hybrid as a bifunctional photocatalyst/adsorbent for CO_2 reduction under visible light irradiation, Chem. Eng. J. 446 (2022), 137003, https://doi.org/10.1016/j.cej.2022.137003.
[60] H. Keller, A. Bussmann-Holder, K.A. Müller, Jahn–Teller physics and high-Tc superconductivity, Mater. Today 11 (2008) 38–46, https://doi.org/10.1016/S1369-7021(08)70178-0.
[61] H.-J. Yin, K. Yuan, Y.-L. Zheng, X.-C. Sun, Y.-W. Zhang, In situ synthesis of NiO/CuO nanosheet heterostructures rich in defects for efficient electrocatalytic oxygen evolution reaction, J. Phys. Chem. C 125 (2021) 16516–16523, https://doi.org/10.1021/acs.jpcc.1c03824.
[62] J. Shi, S. Li, F. Wang, L. Gao, Y. Li, X. Zhang, J. Lu, In situ topotactic formation of 2D/2D direct Z-scheme $Cu_2S/Zn_{0.67}Cd_{0.33}S$ in-plane intergrowth nanosheet heterojunctions for enhanced photocatalytic hydrogen production, Dalton Trans. 48 (2019) 3327–3337, https://doi.org/10.1039/C8DT04154G.
[63] M.R. Islam, J.E. Obaid, M. Saiduzzaman, S.S. Nishat, T. Debnath, A. Kabir, Effect of Al doping on the structural and optical properties of CuO nanoparticles prepared by solution combustion method: experiment and DFT investigation, J. Phys. Chem. Solids 147 (2020), 109646, https://doi.org/10.1016/j.jpcs.2020.109646.
[64] B. Karthikeyan, Raman spectral probed electron–phonon coupling and phonon lifetime properties of Ni-doped CuO nanoparticles, Appl. Phys. A 127 (2021) 205, https://doi.org/10.1007/s00339-021-04330-1.
[65] W. Gou, X. Mo, C. Ren, H. Wang, W. Li, Formation of crystalline multimetallic layered double hydroxide precipitates during uptake of Co, Ni, and Zn onto γ-alumina: evidence from EXAFS, XRD, and TEM, Chemosphere 307 (2022), 136055, https://doi.org/10.1016/j.chemosphere.2022.136055.
[66] P. Lagarde, H. Dexpert, EXAFS in catalysis, Adv. Phys. 33 (1984) 567–594, https://doi.org/10.1080/00018738400101701.
[67] H. Chen, S. He, M. Xu, M. Wei, D.G. Evans, X. Duan, Promoted synergic catalysis between metal Ni and acid–base sites toward oxidant-free dehydrogenation of alcohols, ACS Catal. 7 (2017) 2735–2743, https://doi.org/10.1021/acscatal.6b03494.
[68] J. Li, T. Shen, H. Wang, S. Li, J. Wang, G.R. Williams, Y. Zhao, X. Kong, L. Zheng, Y.-F. Song, Insights into the superstable mineralization of chromium(III) from wastewater by CuO, ACS Appl. Mater. Interfaces 14 (2022) 37823–37832, https://doi.org/10.1021/acsami.2c10298.
[69] H. Wang, W. Zheng, W. Li, F. Tian, S. Kuang, Y. Bu, J.-P. Ao, Control the energy band potential of ZnMgO solid solution with enhanced photocatalytic hydrogen evolution capacity, Appl. Catal. B Environ. 217 (2017) 523–529, https://doi.org/10.1016/j.apcatb.2017.04.079.
[70] P.S. Menon, J. Kunjumon, A.K. Jose, A. P.A, M. Bansal, G. Vinitha, T. Maity, P. M. Abraham, D. Sajan, S.D. George, Structural, third order nonlinear and magnetic properties of pristine and Ni-doped CuO nanoparticles: diluted magnetic semiconductors, Colloids Surf. A Physicochem. Eng. Asp. 650 (2022), 129582, https://doi.org/10.1016/j.colsurfa.2022.129582.
[71] C.T. Meneses, J.G.S. Duque, L.G. Vivas, M. Knobel, Synthesis and characterization of TM-doped CuO (TM=Fe, Ni), J. Non-Cryst. Solids 354 (2008) 4830–4832, https://doi.org/10.1016/j.jnoncrysol.2008.04.025.
[72] S. Yousaf, T. Kousar, M.B. Taj, P.O. Agboola, I. Shakir, M.F. Warsi, Synthesis and characterization of double heterojunction-graphene nano-hybrids for photocatalytic applications, Ceram. Int. 45 (2019) 17806–17817, https://doi.org/10.1016/j.ceramint.2019.05.352.
[73] J. Qian, Q. Hu, X. Hou, F. Qian, L. Dong, B. Li, Study of different Ti/Zr ratios on the physicochemical properties and catalytic activities for CuO/Ti–Zr–O composites, Ind. Eng. Chem. Res. 57 (2018) 12792–12800, https://doi.org/10.1021/acs.iecr.8b02674.
[74] H.J. Yoon, J. Hyun Yang, S.J. Park, C.K. Rhee, Y. Sohn, Photocatalytic CO_2 reduction and hydrogen production over Pt/Zn-embedded β-Ga_2O_3 nanorods, Appl. Surf. Sci. 536 (2021), 147753, https://doi.org/10.1016/j.apsusc.2020.147753.
[75] J. Zhu, S. Zhu, X. Kong, Y. Liang, Z. Li, S. Wu, S. Luo, C. Chang, Z. Cui, Rutile-coated B-phase TiO_2 heterojunction nanobelts for photocatalytic H_2 evolution, ACS Appl. Nano Mater. 3 (2020) 10349–10359, https://doi.org/10.1021/acsanm.0c02263.
[76] M. Xu, C. Sun, X. Zhao, H. Jiang, H. Wang, P. Huo, Fabricated hierarchical CdS/Ni-MOF heterostructure for promoting photocatalytic reduction of CO_2, Appl. Surf. Sci. 576 (2022), 151792, https://doi.org/10.1016/j.apsusc.2021.151792.
[77] P. Chen, L. Chen, Xa Dong, H. Wang, J. Li, Y. Zhou, C. Xue, Y. Zhang, F. Dong, Enhanced photocatalytic VOCs mineralization via special Ga-O-H charge transfer

channel in α-Ga_2O_3/MgAl-LDH heterojunction, ACS ES&T Eng. 1 (2021) 501–511, https://doi.org/10.1021/acsestengg.0c00194.
[78] B. He, Z. Wang, P. Xiao, T. Chen, J. Yu, L. Zhang, Cooperative coupling of H_2O_2 production and organic synthesis over a floatable polystyrene-sphere-supported TiO_2/Bi_2O_3 S-scheme photocatalyst, Adv. Mater. 34 (2022), 2203225, https://doi.org/10.1002/adma.202203225.
[79] Y.-F. Mu, C. Zhang, M.-R. Zhang, W. Zhang, M. Zhang, T.-B. Lu, Direct Z-scheme heterojunction of ligand-free $FAPbBr_3$/α-Fe_2O_3 for boosting photocatalysis of CO_2 reduction coupled with water oxidation, ACS Appl. Mater. Interfaces 13 (2021) 22314–22322, https://doi.org/10.1021/acsami.1c01718.
[80] S. Sato, T. Arai, T. Morikawa, Toward solar-driven photocatalytic CO_2 reduction using water as an electron donor, Inorg. Chem. 54 (2015) 5105–5113, https://doi.org/10.1021/ic502766g.
[81] P. Zhang, Y. Li, Y. Zhang, R. Hou, X. Zhang, C. Xue, S. Wang, B. Zhu, N. Li, G. Shao, Photogenerated electron transfer process in heterojunctions: in situ irradiation XPS, Small Methods 4 (2020), 2000214, https://doi.org/10.1002/smtd.202000214.
[82] Y. Li, L. Wang, F. Zhang, W. Zhang, G. Shao, P. Zhang, Detecting and quantifying wavelength-dependent electrons transfer in heterostructure catalyst via in situ irradiation XPS, Adv. Sci. 10 (2023), 2205020, https://doi.org/10.1002/advs.202205020.
[83] L. Jin, E. Shaaban, S. Bamonte, D. Cintron, S. Shuster, L. Zhang, G. Li, J. He, Surface basicity of metal@TiO_2 to enhance photocatalytic efficiency for CO_2 reduction, ACS Appl. Mater. Interfaces 13 (2021) 38595–38603, https://doi.org/10.1021/acsami.1c09119.
[84] M. Piñón-Espitia, J.A. Torres-Ochoa, O. Córtazar-Martínez, A. Herrera-Gomez, G. Herrera-Perez, M.T. Ochoa-Lara, Charge transfer effects in CuO nanofibers, observed by EELS and XPS, Microsc. Microanal. 26 (2020) 1424–1425, https://doi.org/10.1017/S143192762001805X.
[85] Q. Shi, J. Huang, Y. Yang, J. Wu, J. Shen, X. Liu, A. Sun, Z. Liu, In-situ construction of urchin-like hierarchical g-C_3N_4/NiAl-LDH hybrid for efficient photoreduction of CO_2, Mater. Lett. 268 (2020), 127560, https://doi.org/10.1016/j.matlet.2020.127560.
[86] X. Tong, J. Shou, H. Song, Y. Wang, L. Huang, L. Yin, Ultrafast electron transfer from crystalline g-C_3N_4 to Pt revealed by femtosecond transient absorption spectroscopy, Energy Fuels 268 (2022), 127560, https://doi.org/10.1021/acs.energyfuels.2c01365.
[87] M.A. Khan, P. Maity, M. Al-Oufi, I.K. Al-Howaish, H. Idriss, Electron transfer of the metal/semiconductor system in photocatalysis, J. Phys. Chem. C 122 (2018) 16779–16787, https://doi.org/10.1021/acs.jpcc.8b03741.
[88] T.-H. Lai, K.-i Katsumata, Y.-J. Hsu, In situ charge carrier dynamics of semiconductor nanostructures for advanced photoelectrochemical and photocatalytic applications, Nanophotonics 10 (2021) 777–795, https://doi.org/10.1515/nanoph-2020-0472.
[89] J. Mahl, S. Neppl, F. Roth, M. Borgwardt, C. Saladrigas, B. Toulson, J. Cooper, T. Rahman, H. Bluhm, J. Guo, W. Yang, N. Huse, W. Eberhardt, O. Gessner, Decomposing electronic and lattice contributions in optical pump – X-ray probe transient inner-shell absorption spectroscopy of CuO, Faraday Discuss. 216 (2019) 414–433, https://doi.org/10.1039/C8FD00236C.
[90] B. Shan, B.H. Farnum, K.-R. Wee, T.J. Meyer, Generation of long-lived redox equivalents in self-assembled bilayer structures on metal oxide electrodes, J. Phys. Chem. C 121 (2017) 5882–5890, https://doi.org/10.1021/acs.jpcc.6b12416.
[91] N. Tancogne-Dejean, M.A. Sentef, A. Rubio, Ultrafast transient absorption spectroscopy of the charge-transfer insulator NiO: beyond the dynamical Franz-Keldysh effect, Phys. Rev. B 102 (2020), 115106, https://doi.org/10.1103/PhysRevB.102.115106.
[92] H.T. Xingang Fei, Bei Cheng, Bicheng Zhu, Liuyang Zhang, 2D/2D black phosphorus/g-C_3N_4 S-scheme heterojunction photocatalysts for CO_2 reduction investigated using DFT calculations, Acta Phys. Chim. Sin. 37 (2021), 2010027, https://doi.org/10.3866/pku.Whxb202010027.
[93] Y. Zhao, Y. Lin, G. Wang, Z. Jiang, R. Zhang, C. Zhu, Photocatalytic water splitting of (F, Ti) codoped heptazine/triazine based g-C_3N_4 heterostructure: a hybrid DFT study, Appl. Surf. Sci. 463 (2019) 809–819, https://doi.org/10.1016/j.apsusc.2018.08.013.
[94] Q. Wang, Z. Miao, Y. Zhang, T. Yan, L. Meng, X. Wang, Photocatalytic reduction of CO_2 with H_2O mediated by Ce-tailored bismuth oxybromide surface frustrated Lewis pairs, ACS Catal. 12 (2022) 4016–4025, https://doi.org/10.1021/acscatal.1c05553.
[95] Z. Miao, Q. Wang, Y. Zhang, L. Meng, X. Wang, In situ construction of S-scheme AgBr/BiOBr heterojunction with surface oxygen vacancy for boosting photocatalytic CO_2 reduction with H_2O, Appl. Catal. B Environ. 301 (2022), 120802, https://doi.org/10.1016/j.apcatb.2021.120802.
[96] J. Zhao, Z. Miao, Y. Zhang, G. Wen, L. Liu, X. Wang, X. Cao, B. Wang, Oxygen vacancy-rich hierarchical BiOBr hollow microspheres with dramatic CO_2 photoreduction activity, J. Colloid Interface Sci. 593 (2021) 231–243, https://doi.org/10.1016/j.jcis.2021.02.117.
[97] X. Ren, M. Gao, Y. Zhang, Z. Zhang, X. Cao, B. Wang, X. Wang, Photocatalytic reduction of CO_2 on BiO_X : effect of halogen element type and surface oxygen vacancy mediated mechanism, Appl. Catal. B Environ. 274 (2020), 119063, https://doi.org/10.1016/j.apcatb.2020.119063.
[98] M.L. Ovcharov, A.M. Mishura, N.D. Shcherban, S.M. Filonenko, V.M. Granchak, Photocatalytic reduction of CO_2 using nanostructured Cu_2O with foam-like structure, Sol. Energy 139 (2016) 452–457, https://doi.org/10.1016/j.solener.2016.10.010.